remote sensing

MDPI

Article

Integrated Geophysical Approach of Groundwater Potential in Wadi Ranyah, Saudi Arabia, Using Gravity, Electrical Resistivity, and Remote-Sensing Techniques

Ahmed Mohamed [1,†], Abdullah Othman [2,†], Wael F. Galal [1] and Ahmed Abdelrady [3,*]

[1] Geology Department, Faculty of Science, Assiut University, Assiut 71516, Egypt
[2] Department of Environmental Engineering, Umm Al-Qura University, Makkah 24382, Saudi Arabia
[3] Faculty of Civil Engineering and Geoscience, Delft University of Technology, 2629 HS Delft, The Netherlands
* Correspondence: a.r.a.mahmoud@tudelft.nl
† Co-first author, these authors contributed equally to this work.

Abstract: In order to cope with the rise in human-caused demands, Saudi Arabia is exploring new groundwater sources. The groundwater potential of Wadi Ranyah was studied using a multi-dataset-integrated approach that included time-variable gravity data from the Gravity Recovery and Climate Experiment (GRACE), vertical electrical sounding (VES), and time-domain-electromagnetic (TDEM) data with other related datasets to examine the variations and occurrence of groundwater storage and to define the controlling factors affecting the groundwater potential in Wadi Ranyah in southwestern Saudi Arabia. Between April 2002 and December 2021, the estimated variation in groundwater resources was -3.85 ± 0.15 mm/yr. From 2002 to 2019, the area observed an average yearly precipitation rate of 100 mm. The sedimentary succession and the underlying fractured basement rocks are influenced by the structural patterns that run mainly in three different trends (NW, NE, and NS). The sedimentary cover varies from 0 to 27 m in thickness. The outputs of the electrical sounding revealed four primary geoelectric units in the study area: on top, a highly resistant geoelectrical unit with a resistivity of 235–1020 Ω.m, composed of unsorted, loose, recent sediments; this is followed by a layer of gravel and coarse-grained sands with a resistivity of 225–980 Ω.m; then, a water-bearing unit of saturated sediments and weathered, fractured, basement crystalline rocks with a resistivity of 40–105 Ω.m, its depth varying from 4 to ~9 m; and then the lowest fourth unit composed of massive basement rocks with higher resistivity values varying from 4780 to 7850 Ω.m. The seven built dams store surface-water runoff in the southwestern part of the wadi, close to the upstream section, in addition to the Ranyah dam, as the eighth one is located in the middle of the wadi. The subsurface NW- and NS-trending fault lines impede the groundwater from flowing downstream of the wadi, forming isolated water-bearing grabens. Minimal surface runoff might occur in the northern part of the wadi. The combined findings are beneficial because they provide a complete picture of the groundwater potential of Wadi Ranyah and the controlling structural patterns. Using this integrated technique, the groundwater potential in arid and semiarid regions can now be accurately assessed.

Keywords: gravity data; VES; TDEM; groundwater resources; depletion; Wadi Ranyah; Saudi Arabia

Citation: Mohamed, A.; Othman, A.; Galal, W.F.; Abdelrady, A. Integrated Geophysical Approach of Groundwater Potential in Wadi Ranyah, Saudi Arabia, Using Gravity, Electrical Resistivity, and Remote-Sensing Techniques. *Remote Sens.* **2023**, *15*, 1808. https://doi.org/10.3390/rs15071808

Academic Editors: Jolanta Nastula and Monika Birylo

Received: 14 February 2023
Revised: 17 March 2023
Accepted: 22 March 2023
Published: 28 March 2023

1. Introduction

Human activities have increased the effects of climate change on the regional water balance and water storage [1,2]. The depletion of water storage is a major problem in many regions of the world, especially in arid and/or semi-arid areas [3]. A landmass's overall water supply, comprising all of its liquid water forms (surface, soil, ground, etc.), is referred to as its terrestrial water storage (TWS). It is highly sensitive to environmental changes but plays an important part in the energy and water cycles, as well as the biochemical cycle. Measuring the spatial and temporal fluctuations of the TWS and its hydrological

components, evaluating the severity of hydrological droughts (e.g., [4]), and identifying its primary driving reasons are all necessary for effective water-resource management in dry regions.

Groundwater is an important water resource for supporting life and maintaining agricultural and commercial activity in semi-arid and dry settings, and it is thus critical for socioecological sustainability. However, groundwater storage in these places is being depleted because of climate change and heavy human activity, endangering the ecosystem's stability and security [5]. Thus, there is an immediate need for a comprehensive and trustworthy groundwater resource assessment. Accurate groundwater-storage variation aids policymakers in gaining a scientific understanding of efficient water-resource planning and management [6], which is critical in water-scarce deserts and semi-arid regions.

Physical and chemical models have long been employed on the groundwater level to assess the aquifer systems' rates of recharging, discharging, and depleting, as well as investigating the interconnectivity of their sub-basins [7–12]. Given the scarcity of the datasets needed for their application and the considerable time and resources needed to gather them, these methodologies are challenging to apply at regional level, and their conclusions are frequently disputed [13]. Additionally, in areas with complicated underlying conditions or limited hydrogeological data, the requirement for various hydrogeological components, particularly as initial and boundary requirements for the partial and normal differential equations, is a challenging task [14]. Furthermore, when simplified controlling equations are used to describe the real hydrogeological system, it is difficult to quantify the uncertainty of the results [15,16]. Given the restricted availability of the datasets required for the implementation of these mathematical equations, as well as the extensive time and resources required to acquire them, their results are sometimes doubtful and their regional application is challenging [13].

In dry, poorly populated locations, it would be impractical to conduct TWS observations on the ground. TWS simulation using hydrological models is challenging due to a lack of input data. Since the launch of the Gravity Recovery and Climate Experiment (GRACE) on 17 March 2002, it has monitored the variations in Earth's gravitational field [17,18]. GRACE's time-variable gravity-field data have been used to expose the gravity-altering impacts of big earthquakes [19,20], estimate ice-mass losses [21,22], quantify recharging and depletion rates [23–30], estimate groundwater-storage changes across large areas [31–36], integrate with other electrical resistivity data to assess the groundwater occurrence regionally and locally [37,38], assess sea-level variations [39,40], and put a numerical value on TWS shifts [39,41]. Despite the fact that GRACE was retired in 2017, the follow-up GRACE Follow On (GRACE-FO) mission started in 2018 to continue providing time-variable gravity-field data.

It is commonly known that there has been a serious water shortage in the Middle East, and that conflicts have frequently broken out over the region's meager resources [37,42–44]. Saudi Arabia is one of the nations that needs quick and widespread attention. The agricultural and industrial sectors in Saudi Arabia have both witnessed significant growth in recent years. Additionally, the increased demand for water is a direct effect of the rapid population increase. No natural bodies of surface water exist there, and the average annual precipitation (AAP) is less than 100 mm, making this a desert environment [45,46]. Therefore, numerous investigations in Saudi Arabia have focused on the different water fields (e.g., [47,48]).

Despite the fact that 99.84% of Saudis have access to drinkable water [49], Saudi Arabia is considered one of the driest countries in the world. Absolute water scarcity is 500 m^3/cap./yr, while Saudi Arabia has just 89 m^3/cap./yr [50]. Geoelectrical methods have been used to estimate the electrical properties of concealed formations. Insight into the geoelectrical layers and structures below the surface, as well as the presence of groundwater, can be obtained from these observations [51,52].

The vertical-electrical-sounding (VES) technique was extensively utilized to detect subsurface cavities, cracks, and fissures, and it has also been utilized in groundwater

exploration and pollution monitoring [53], the freshwater-saline contact zone [54], and water-relevant variables [55,56]. DC-geoelectric soundings were conducted in the salt mine Asse as part of research into the disposal of radioactive waste in 1982. The survey's findings led to the identification of various salt formations' resistivities. It can be determined using Archie's equation how much free water is present in salt by comparing various resistivities found in salt formations in the mine [57]. The resistivity method has been successfully used to evaluate the depth to groundwater and the thickness of cracked hard-rock formations [58], as well as to investigate the aquifer and groundwater resources [59,60]. Moreover, contaminated groundwater zones affect the electrical resistivity method [61]. Furthermore, it has been used with borehole data to predict the geohydraulic characteristics of Abi's fractured shale and sandstone aquifers [62].

The time-domain-electromagnetic (TDEM) method is a geophysical technique that utilizes electromagnetic induction to study the resistivity of subsurface materials as a function of depth. It works by generating a primary magnetic field on the surface and measuring the decay of a secondary magnetic field induced in the subsurface. This method is particularly useful for detecting conductive layers, as it is sensitive to the currents induced in these layers. The depth of investigation using TDEM depends on the resistivity of the subsurface materials, with higher resistivity resulting in faster diffusion of the secondary field and vice versa [63].

Wadi Ranyah (Figure 1) in southwestern Saudi Arabia served as a local site due to its proximity and agricultural growth, and the residential uses of its groundwater. The research aimed to: (1) quantify the spatiotemporal fluctuations of TWS in the watershed basin of the wadi from April 2002 to December 2021, and identify the main controlling factors on groundwater occurrence; (2) study the subsurface layers and structural trends affecting the occurrence of the groundwater; (3) estimate the depth-to-groundwater level; and (4) study the effects of surface runoff on the replenishment of groundwater resources of the Wadi Ranyah. These findings will be used to manage the groundwater resources and identify the most suitable locations for boreholes within the region, in addition to addressing the lack of freshwater resources. The implementation of these measures will also help ensure the long-term sustainability of the water supply for the communities of Wadi Ranyah.

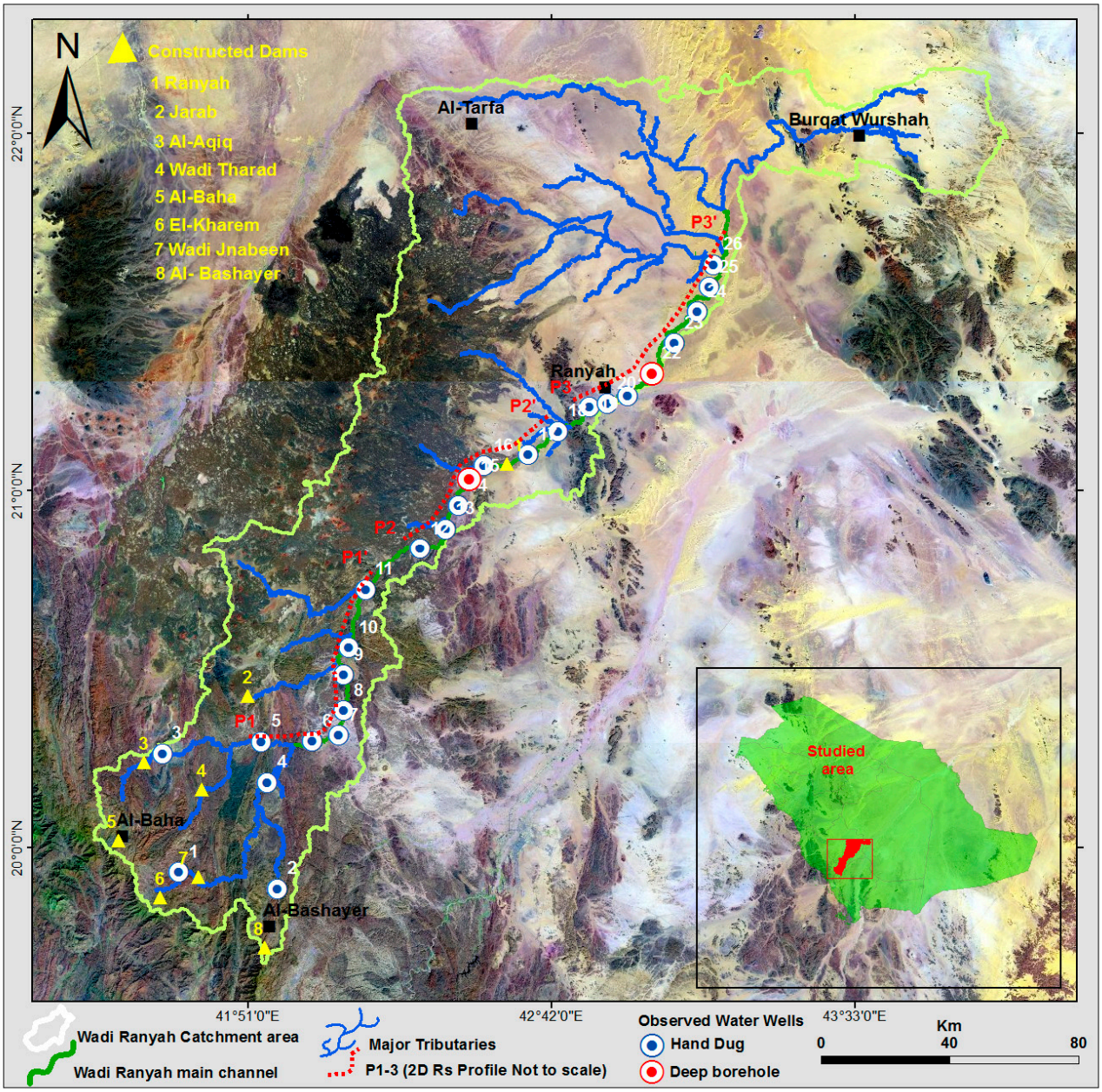

Figure 1. Location map of Wadi Ranyah showing the catchment area, main channel, boreholes, resistivity profiles, and constructed dams.

2. Geology

Wadi Ranyah is a significant geological feature that is located in the Arabian Shield of southwestern Saudi Arabia. This endorheic or inland wadi, which stretches from the Baha Mountains in the southwest to the northeast, has a main channel that is approximately 245 km long, making it one of the longest in the region.

The geology of Wadi Ranyah is exposed by a range of rock units from the Precambrian to Quaternary periods, as depicted in Figure 2. These rock units include metamorphic basalt, andesite and basaltic flows, pyroclastic dacite and rhyolite, metamorphosed volcanic wacke and sandstone, granodiorite, diorite, granitic plutons, gneiss, and schist. Quaternary alluvial strata in the region consist of layers of gravel, eolian sands, silts, and clayey sands that have been eroded from surrounding basement exposures and accumulated in the Wadi Ranyah, with thicknesses ranging from 5–10 m upstream to 10–15 m or more downstream. These strata have high permeability, which affects surface runoff due to their role as a

shallow groundwater-storage basin. In certain areas of the mainstream and tributaries of Wadi Ranyah, highly weathered and fractured hard rocks are exposed on the wadi floor, creating an ideal substrate for shallow groundwater storage.

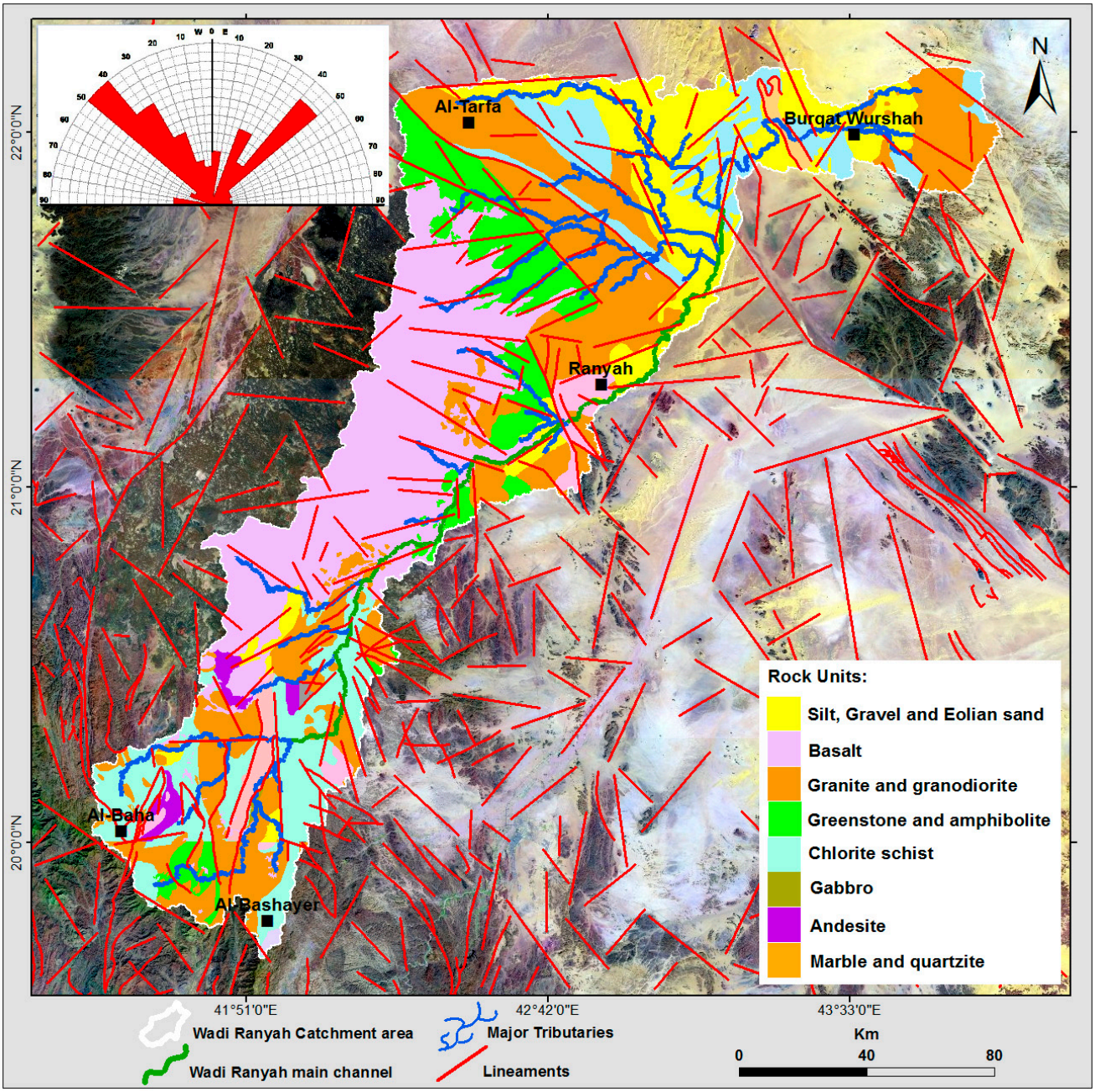

Figure 2. Geological map of the studied area (modified after [64]).

Topographically, the upstream elevation of Wadi Ranyah in Baha ranges from 1750 to 1880 m above the mean sea level (amsl) in the high apparent stream areas, before gradually decreasing downstream (Figure 3). In the northeast, the elevation drops to about 857 m-amsl. The Wadi Ranyah stream network starts with a steep slope in the Baha Mountains and flows downstream, with the slope gradually decreasing along the way (Figure 4).

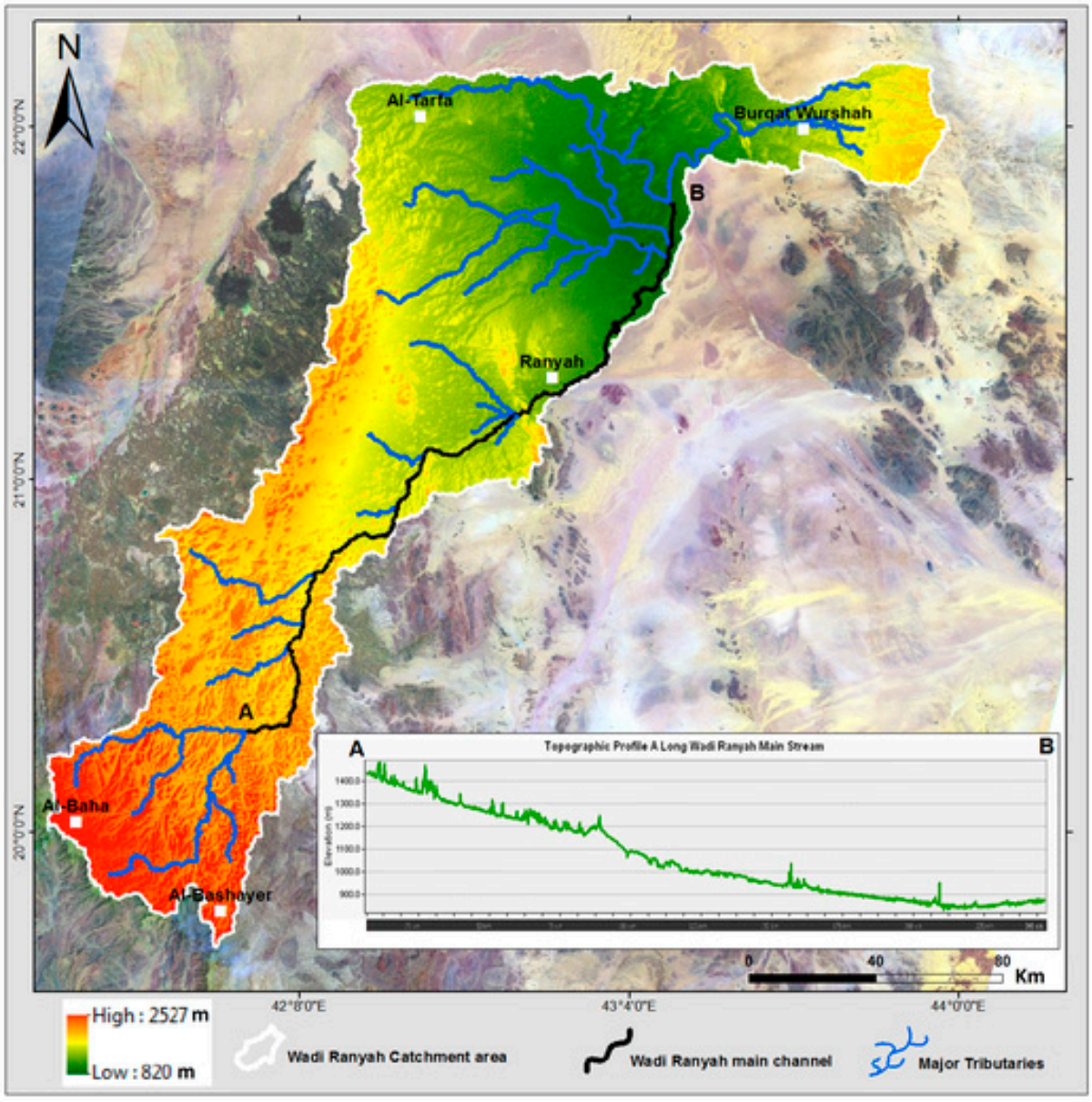

Figure 3. Topographic map with a topographic profile (AB) of the studied area.

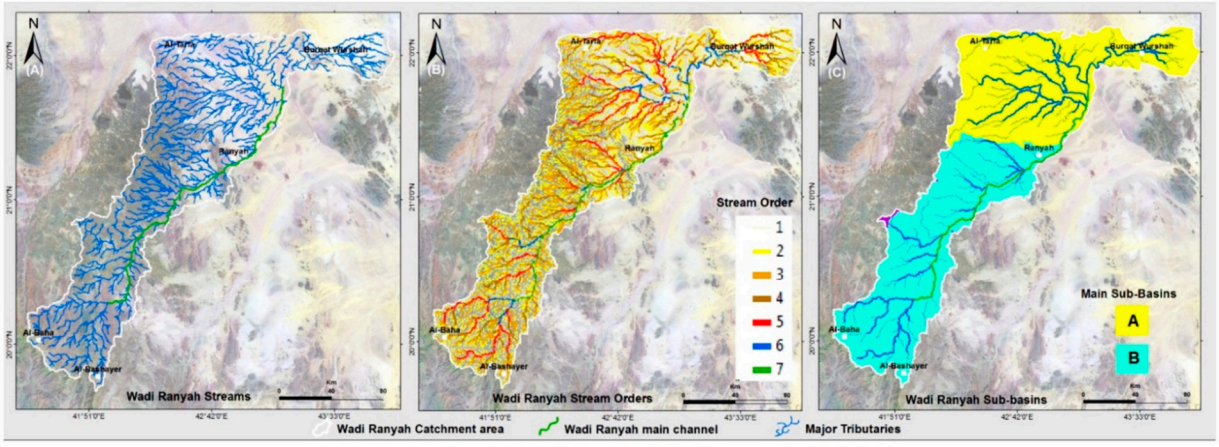

Figure 4. Wadi Ranyah streams (**A**), stream order (**B**), and sub-basins (**C**).

3. Data and Methods

3.1. GRACE Mascon Data

NASA and the German Aerospace Center developed the satellite GRACE gravity mission in collaboration. This satellite mission detects TWS anomalies based on the proportionate link between gravity and earth density [65] by monitoring the gravitational changes on Earth. Here, we utilized the most recent GRACE RL06 datasets covering the period of April 2002–December 2021 in the investigation. The GRACE Mass Concentration blocks (mascon) solution (CSR-RL06M v02 solution; CSR-M) limited the inversion of the satellite range rates to gravity fields by means of time-variable regularization [66,67] released by the Center of Space Research (CSR: http://www2.csr.utexas.edu/grace, accessed on 7 December 2022) with $0.25^\circ \times 0.25^\circ$ grids, which was calculated using an identical area and a resolution of one degree. The Jet Propulsion Laboratory (JPL) released the JPL-RL06M v02 solution and included calculations for TWS anomalies for each equal-area $3^\circ \times 3^\circ$ spherical cap mascon block ([68–70]: http://grace.jpl.nasa.gov, accessed on 7 December 2022). The produced dataset consists of a sampling of TWS variations on 0.5° longitude and latitude grids. Along with the mascon datasets from JPL and CSR, the NASA Goddard Space Flight Center (GSFC-RL06v1.0) mascon solution was computed for every 0.5° equal-area square mascon. This version of the TWS product was acquired using the mascon approach, which considerably improves the spatial resolution of the product and enables its direct use without postprocessing. Smoothing or destriping is unnecessary. Furthermore, certain products may not even require the scaling factor [66,68,69,71,72]. The missing monthly data between April 2002 and June 2017 has been reconstructed using a linear interpolation method [31,73]. Each TWS time series was simultaneously fitted with a trend and a seasonal term, allowing us to extract the secular trend. This method then estimates the errors associated with the produced trend values.

3.2. GLDAS Data

Land-surface models (LSMs) such as the VIC, CLM, Mosaic, and Noah are all incorporated into the Global Land Data Assimilation System (GLDAS), a land-surface simulation system that uses data-assimilation techniques to merge field- and space-based high-resolution observations into a combined model [74]. This study utilized three LSMs (CLM, Noah, and VIC) from GLDAS. This is due to the lack of vertical resolution of the GRACE and its inability to distinguish between the different components of TWS. We only used the soil-moisture-storage variations (SMS) to estimate changes in groundwater storage, due to the absence of other TWS components in the study area. The monthly data used in this investigation covered the same time frame as the GRACE data and had a one-degree spatial resolution.

3.3. TRMM Data

NASA and Japan's National Space Development Agency collaborated on the Tropical Rainfall-Measuring Mission (TRMM), a spacecraft that measures tropical and subtropical precipitation and the energy release that goes along with it. We used TRMM data to assess the effect of precipitation on the wadi's groundwater resources. Given that the Wadi Ranyah lacks rain-gauge stations, and those that do exist are either located in inconvenient locations or do not cover areas with unusually heavy precipitation, the monthly rainfall and average annual rainfall estimates were extracted from the TRMM data over the study area.

3.4. VES and TDEM Data

The electrical resistivity method was chosen for this study because it is widely used in hydrological investigations by imaging the subsurface beneath the wadi deposits and the potentially fractured hard basement rocks. Electrical resistivity is a geophysical technique that measures the apparent resistivity values of subsurface media in both the lateral and vertical directions. The variations in these measured resistivity values provide insight into the complex geological and hydrogeological conditions, including the detection and delim-

itation of groundwater layers [75]. This method is highly versatile and can be effectively utilized to better understand the subsurface conditions in the study area.

The TDEM sounding method has enhanced the depth resolutions for locating water-bearing zones with higher conductivity than surrounding dry layers. Given its higher vertical resolution and lesser susceptibility to geologic distortions, this technique is utilized to identify changes in vertical resistivity [76].

In electromagnetic processes, a primary magnetic field is produced by feeding an electrical current via a transmitter loop and permitting it to propagate into a subterranean medium. Secondary magnetic fields are generated over time by eddy currents in electrically conductive bodies and are returned on the receiving loop. The decay rate of these secondary fields on the receiving loop is measured and analyzed in terms of resistivity variation with depth, providing information on conductive zones and conductivity-contrast interfaces [77].

Measurements were made utilizing the optimal field curve with a high signal-to-noise ratio in order to analyze and interpret the results. According to the Occam's inversion principle, the resulting TDEM data were processed, inverted, and presented as apparent resistivity versus time [78].

3.5. Field Measurements

As part of this research, a total of 41 VES measurements and 9 TDEM measurements were performed along the mainstream of Wadi Ranyah and organized into three main profiles: P1–P1′, P2–P2′, and P3–P3′ (Figure 1). These profiles were positioned parallel to the regional strike of the dipping sediments, rock units, and basement, in a southwest–northeast direction. The resistivity measurements were taken using a Syscal Pro resistivity meter from IRIS and a Shlumberger array with a maximum AB/2 of 200 m, and the resistivity data were inverted and interpreted using the IPI2win [79] software. The TDEM survey was carried out using the TDEM FAST 48 instrument with a loop size of 50 m, and the [80] software was used to process the obtained TDEM field data. The interpreted data were visualized as 2D vertical electrical resistivity sections to clarify the subsurface geological and hydrological framework and verified against the borehole data. A total of 26 groundwater boreholes were inventoried and considered at the site, including 24 hand-dug wells with depths ranging from 12 to 30 m and two deep tube wells with a depth of 100 m, as shown in Figure 1.

3.6. Landsat and SRTM Data

Landsat images with 15 and 30 m resolution issued by [81] were used to produce the geological map and identify surface geological lineaments in the region. A digital elevation model (DEM) V.2 with a resolution of 30 m, issued by the NASA Shuttle Radar Topography Mission [82] in 2013, was used to generate a high-resolution digital topographic map, as well as maps of the surface stream network and watersheds (Figures 3 and 4) (e.g., [83]). Automatic extraction techniques were applied to extract the lineaments from the remote-sensing data [84]. A number of different strategies for extracting lineages with the help of computers have been presented. We extracted the surface lineaments automatically by the most widely applicable PCI Geomatica's LINE module [85]. Using the trend-analysis method, the trends of surface-lineament lines were examined based on their lengths, abundance, and azimuth magnitude. Finally, ESRI ArcGIS 10.5 [86] was used to interpret and map all the spatial data obtained.

4. Result and Discussion

In this work, we integrate various datasets and measurements to take a broad look at the groundwater potential of Wadi Ranyah that is located in the southwestern region of Saudi Arabia.

4.1. Average Annual Precipitation (AAP)

Figure 5a shows a graph of the monthly rainfall rate, which shows higher values for the months of October to April, and lower values for the months of May to September. Figure 5b shows a time series of the average yearly rainfall, with the year 2016 having the highest rate (196.26 mm) and 2008, 2011, 2014, and 2015 having the lowest rate (<66 mm). From the AAP map (Figure 5c), we can see that the eastern part of the wadi has minimal values of about 52.23 mm, while the southwestern parts have slightly higher values up to 120–277 mm. The AAP rate was calculated at 100 mm/yr for the study region throughout the entire study period, which indicates the dryness of the region.

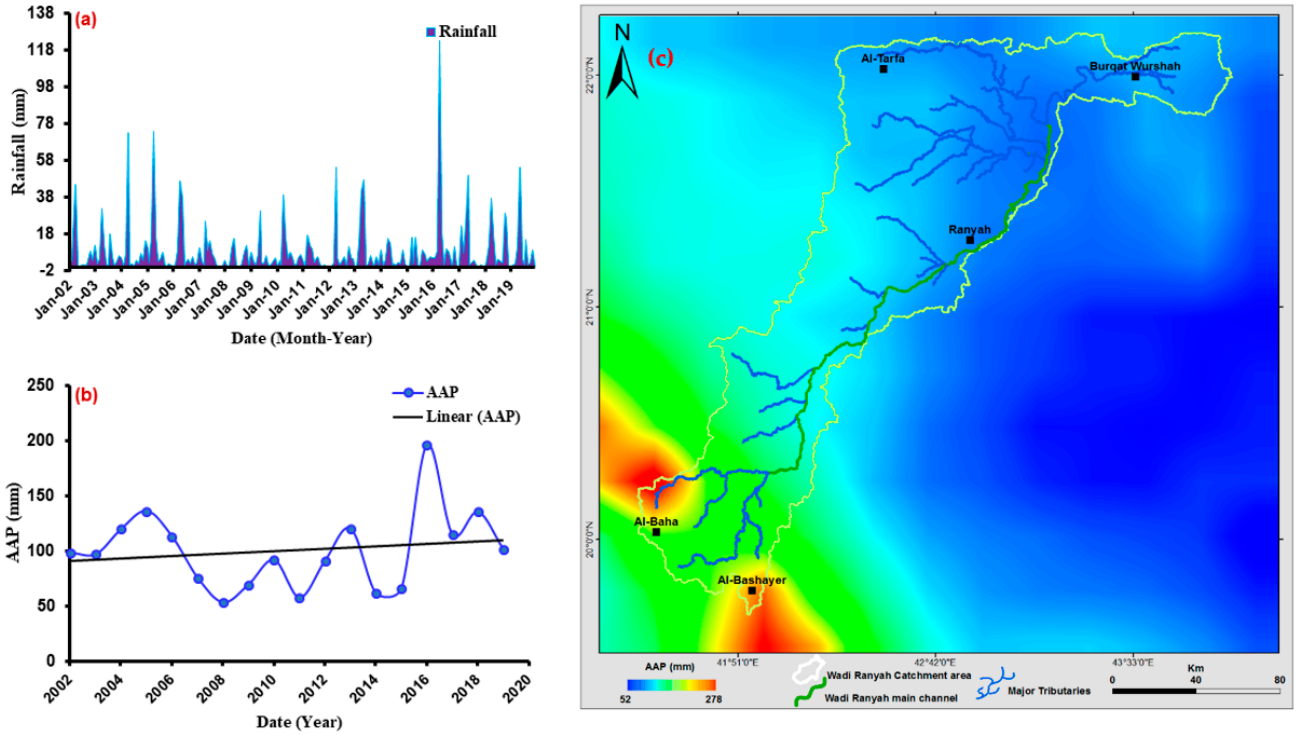

Figure 5. (**a**) Monthly average rainfall (mm), (**b**) the AAP times series, and (**c**) the AAP calculated using TRMM data for the study region.

4.2. ΔTWS and ΔGWS in the Wadi Ranyah Region

The calculated secular TWS trend from 2002 to 2021 using CSR solution is shown spatially in Figure 6a. Figure 6b displays the spatial variations in the average TWS values over the study area for each year. The averages of the various GRACE solutions demonstrate good agreement in amplitudes and phases over the studied region. The datasets covering the study area show correlation coefficients varying between 0.73 and 0.83 (Figure 7). As shown in Figure 6a, the ΔTWS trend exhibits higher negative values in the eastern part of the study area, close to the downstream area of the wadi, while it shows slightly negative values in the southwestern part, close to the upstream area of the wadi. This is evidenced by the higher rainfall amounts over the southwestern region in comparison to the lower amounts over the eastern region, as well as the storage of runoff and precipitation by the constructed dams in the southwestern part of the wadi, which started in 2007.

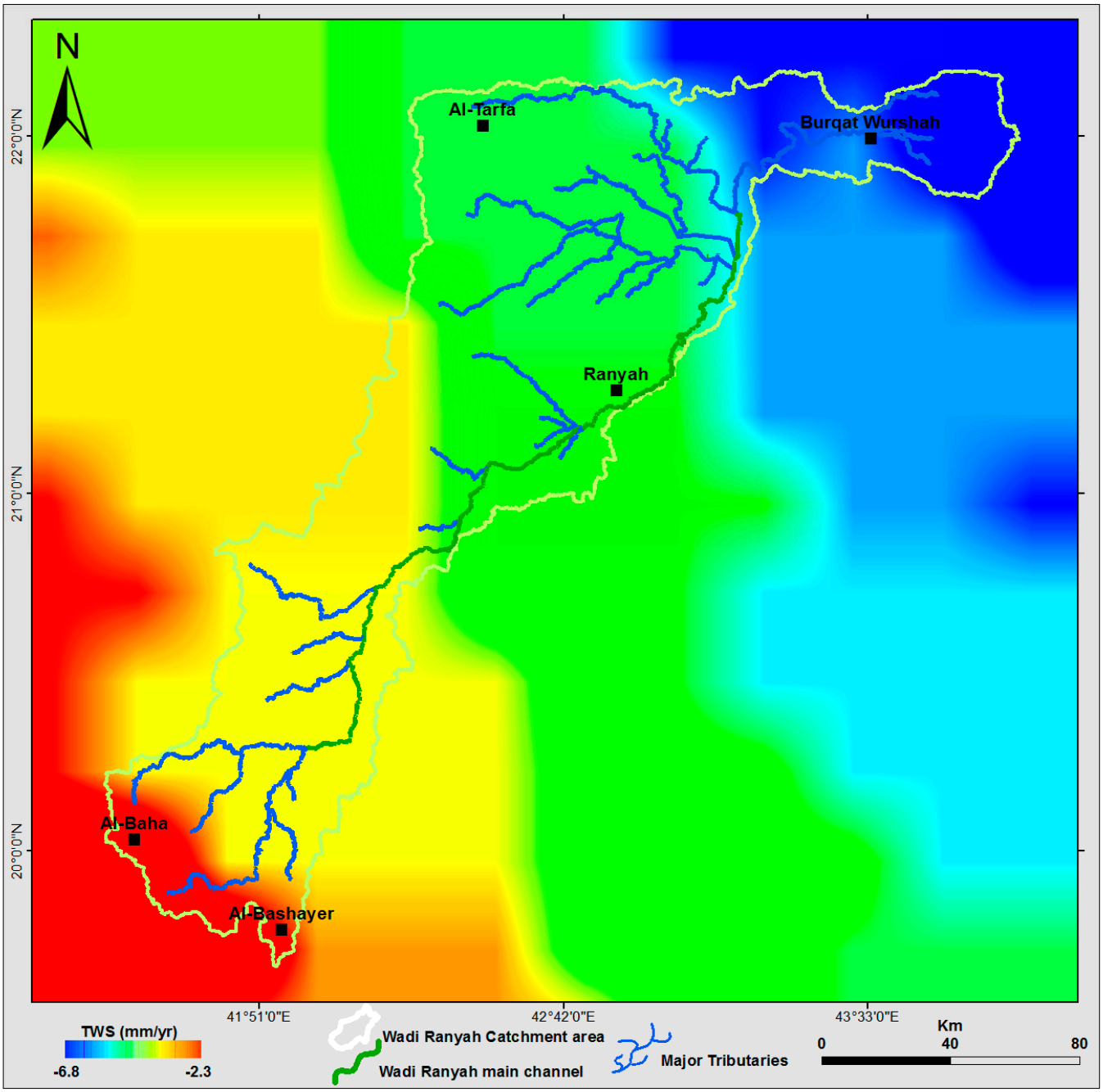

(**a**)

Figure 6. *Cont.*

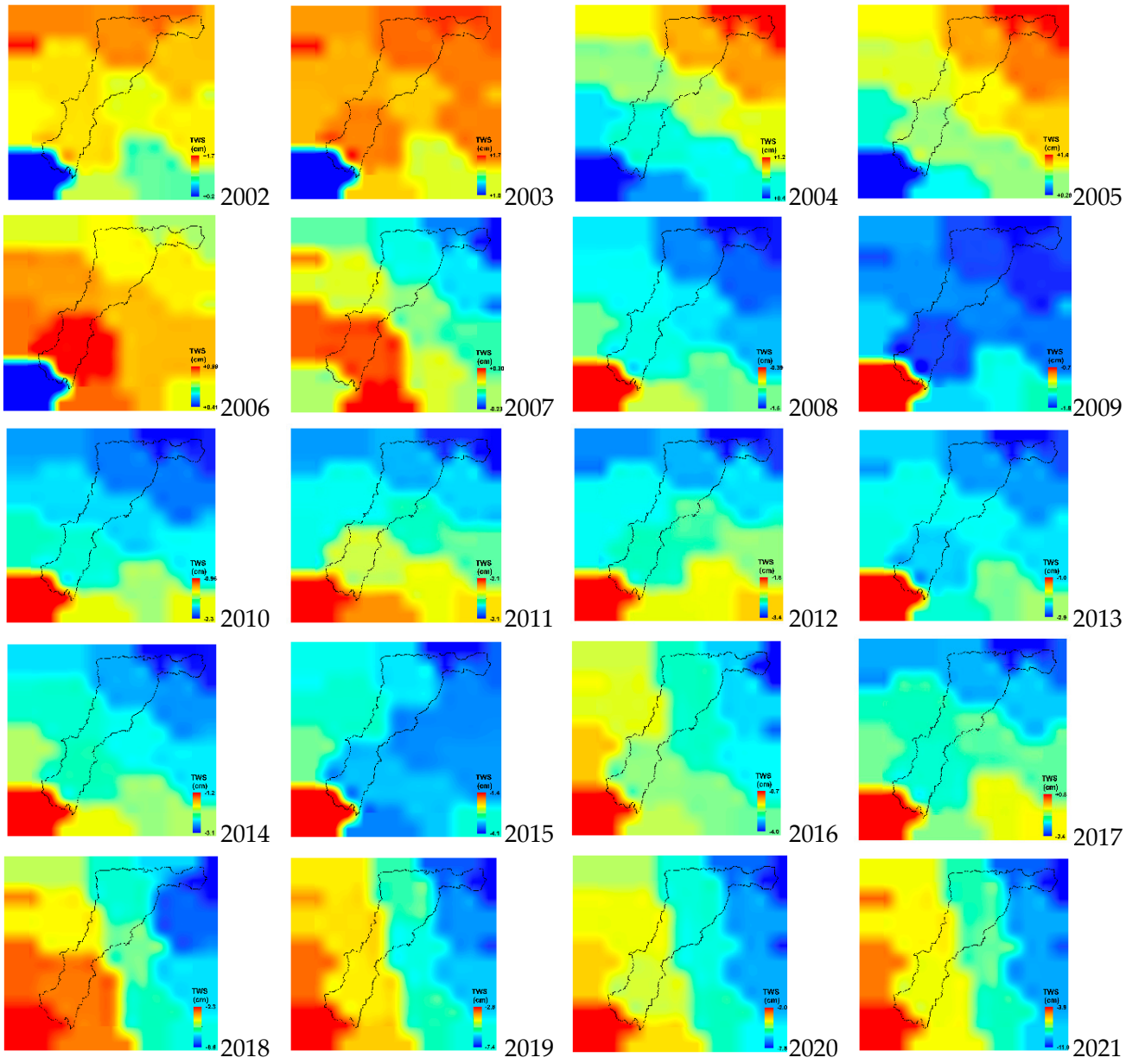

Figure 6. (**a**). Spatiotemporal variations in GRACE-derived ΔTWS trend for the study area derived from mascon CSR solutions. (**b**). Spatial variations in the average GRACE-derived TWS values for the study area derived from mascon CSR solutions between 2002 and 2021.

Figure 8a displays the monthly TWSA time series for Wadi Ranyah from 2002 to 2021 using the three mascon solutions. The change in TWSA is the water storage's derivative with respect to 171 months. During this period, the Wadi Ranyah region's TWSA dropped at a rate of -3.94 ± 0.18, -3.99 ± 0.19 and -3.62 ± 0.22 mm/yr using CSR, GSFC, and JPL mascon solutions, respectively (Table 1). The averaging of TWS (Figure 8b) was computed to be -3.85 ± 0.15 mm/yr for the region.

Long-term variation in ΔSMS trends over the Wadi Ranyah region is shown in Figure 9. The SMS shows an average value of -0.007 ± 0.002 mm/yr for the region. An estimate of the groundwater storage fluctuation was calculated using Equation (1):

$$\Delta TWS = \Delta GWS + \Delta SMS \quad (1)$$

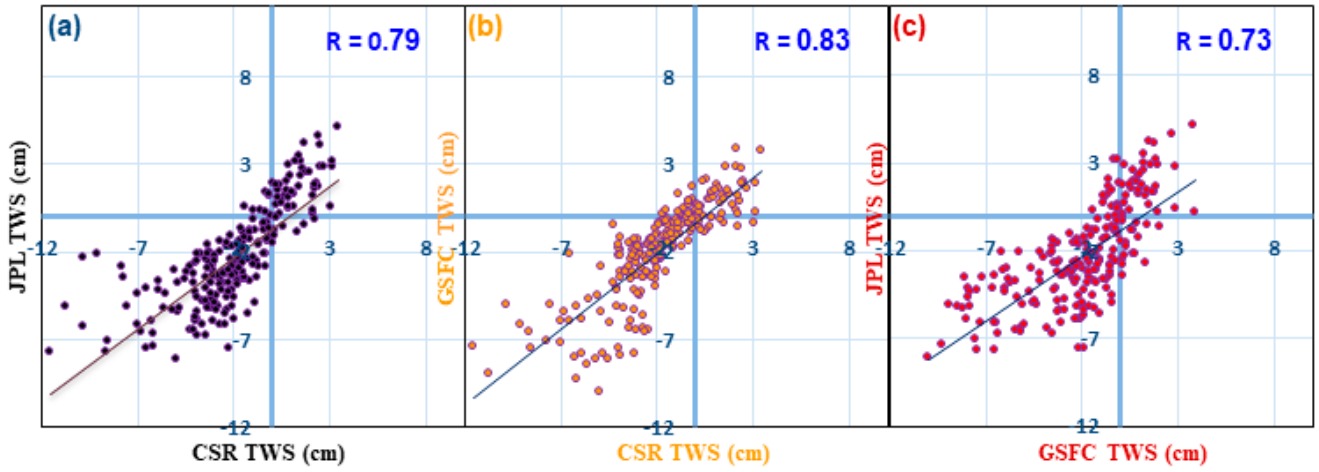

Figure 7. Correlation coefficient (R) between ΔTWS data from the averaging of JPL and CSR mascon solutions (**a**); GSFC and CSR mascon solutions (**b**); and JPL and GSFC mascon solutions (**c**) over the wadi region.

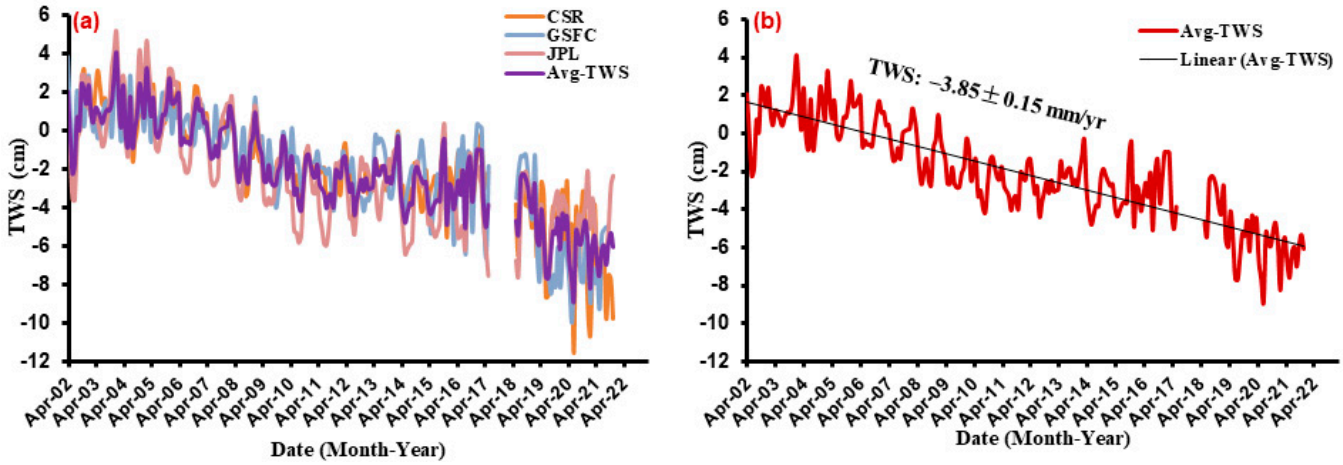

Figure 8. Monthly TWS (**a**) and their mean ΔTWS (**b**) time series from 04/2002 to 12/2021, produced from CSR, GFCF, and JPL GRACE mascon solutions for the study area.

Table 1. ΔTWS components (mm yr^{-1}) over the entire Makah region at a 95% level of confidence.

Component (mm)		Entire Period
GRACE Total (ΔTWS)	CSR	−3.94 ± 0.18
	GSFC	−3.99 ± 0.19
	JPL	−3.62 ± 0.22
	AVG	−3.85 ± 0.15
ΔSMS		−0.007 ± 0.002
ΔGWS		−3.85 ± 0.15
AAP		100

Several researchers have used this equation to predict changes in groundwater storage (e.g., [13,87–89]). The monthly GWS time series shows similar patterns to those of TWS time series (Figure 10a). The computed average ΔGWS trend value (Table 1) for the study region is −3.85 ± 0.15 mm/yr (Figure 10b).

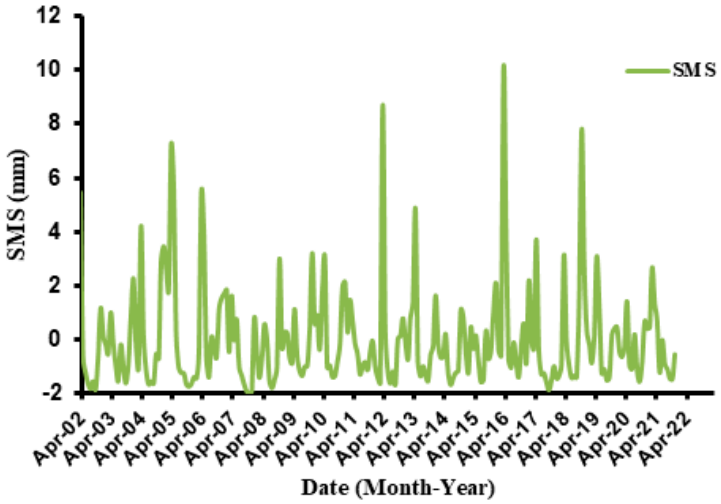

Figure 9. Monthly ΔSMS time series for the study area.

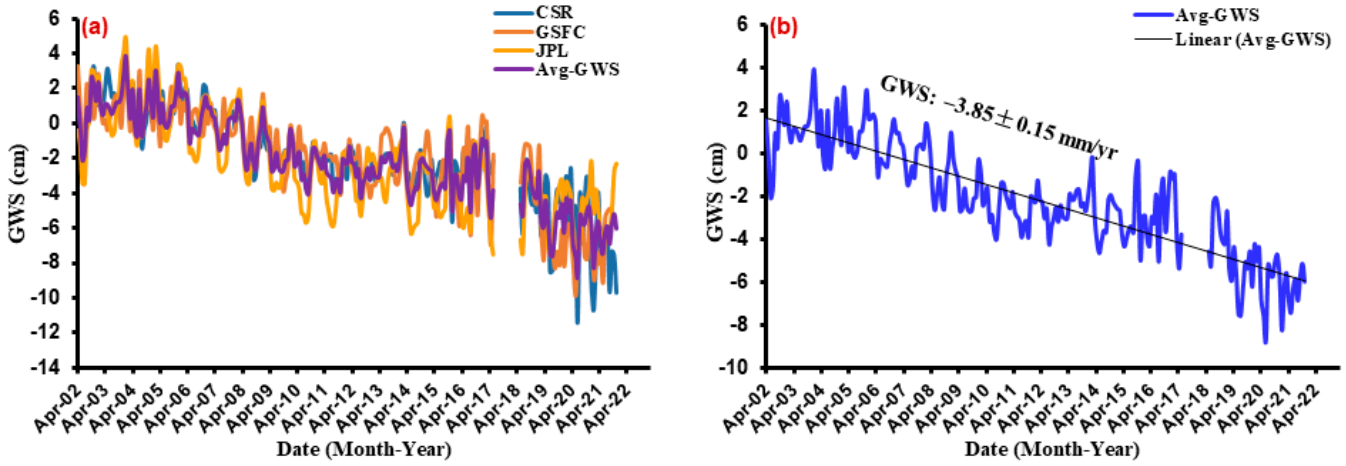

Figure 10. Monthly time series for the GWS (**a**) and their mean ΔGWS (**b**) for the study area.

4.3. Resistivity Results

Three geoelectrical cross-sections (P1–P1′, P2–P2′, and P3–P3′; Table 2) were generated using the results of the inverted VES and TDEM sounding data that displayed the apparent resistivity variations in the subsurface. These cross-sections were used to reveal the continuity or discontinuity in stratigraphic units, the depth and thickness of water-bearing layers, and other subsurface features. The interpretation of the data considered the lithological logs of nearby hand-dug and tube wells. A comparative study of the geoelectric sections and the drilled wells was also conducted to further aid in interpretation.

Table 2. Resistivity (Ω m) and thickness (m) of the subsurface geoelectric layers along Wadi Ranyah profiles.

Profile	P1–P1′		P2–P2′		P3–P3′	
Layer	Resistivity (Ω m)	Thickness (m)	Resistivity (Ω m)	Thickness (m)	Resistivity (Ω m)	Thickness (m)
1st Layer (Upper)	440–1020	1.5–4	235–850	2–4	345–985	3–4
2nd Layer	310–980	2.5–5	225–760	4–4.5	275–740	2.5–5
3rd Layer	40–120	3–7.5	65–105	9–16	55–115	8–16.5
4th Layer (Lower)	850–5200	-	780–4050	-	800–7850	-

Colors are related to the same colors of layers in Figures 11–13.

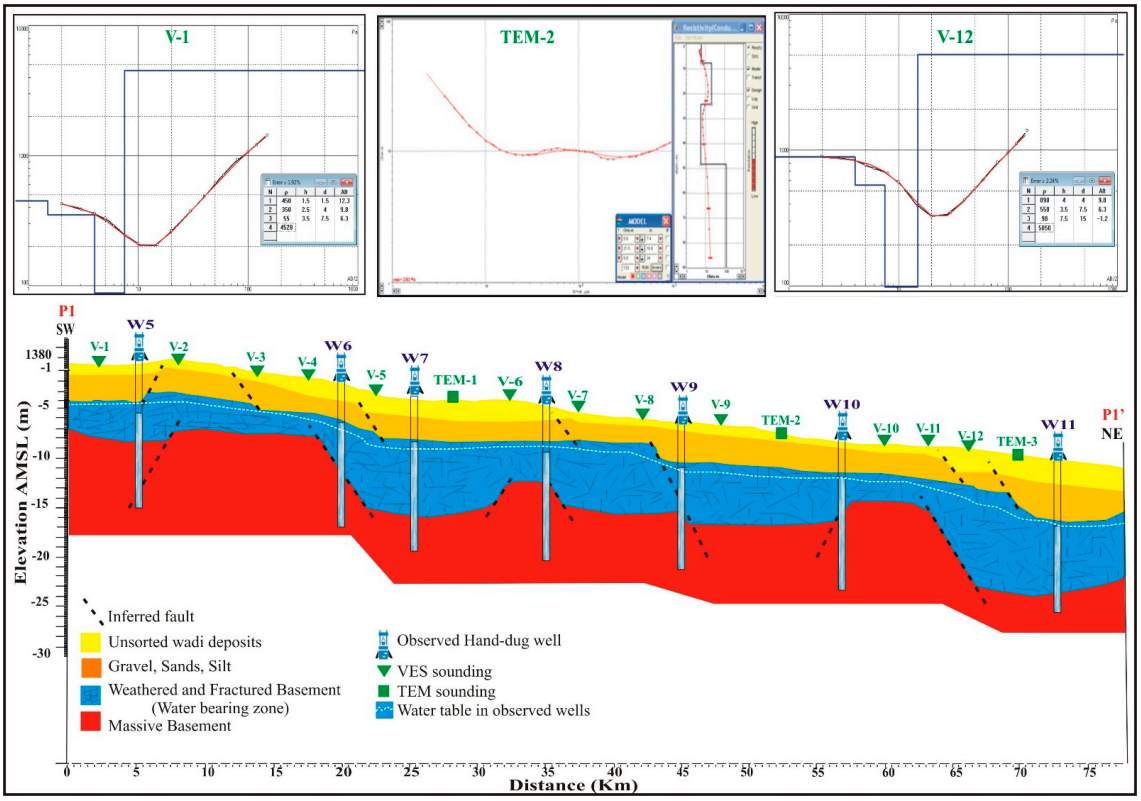

Figure 11. The geoelectric cross-section P1–P1′, with the sounding and the modeled data of VES (V-1, and V-12) and TEM-2.

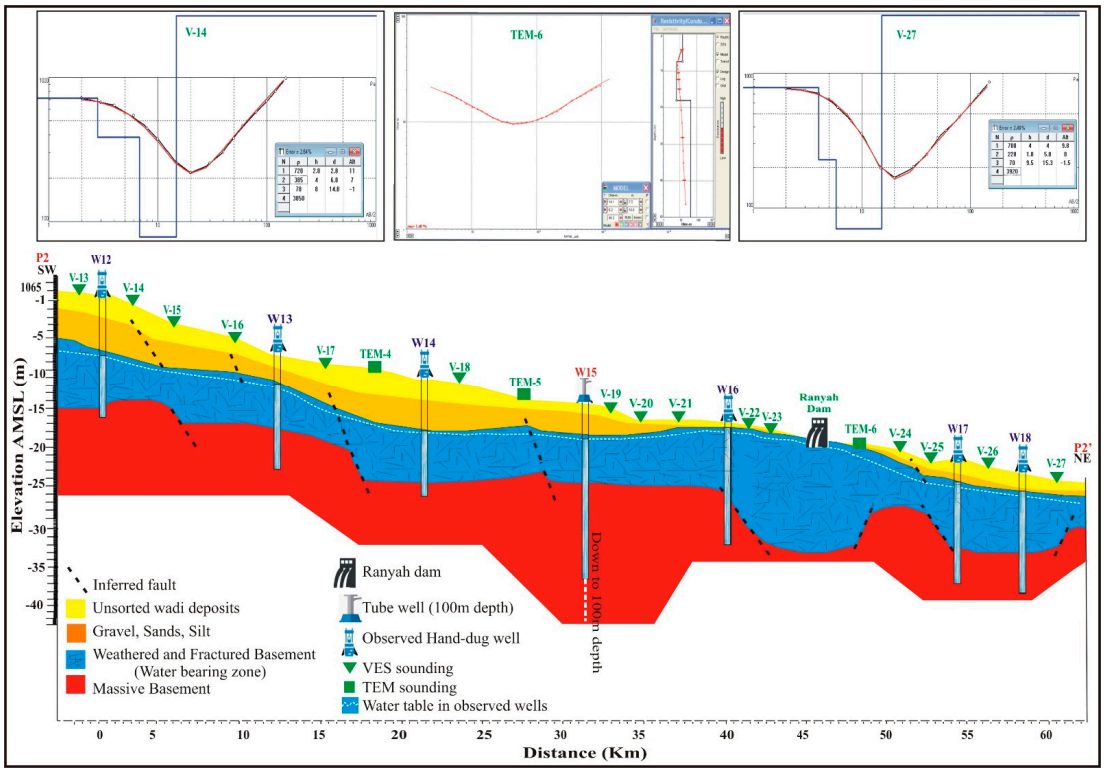

Figure 12. The geoelectric cross-section P2–P2′, with the sounding and the modeled data of VES (V-14, and V-27) and TEM-6.

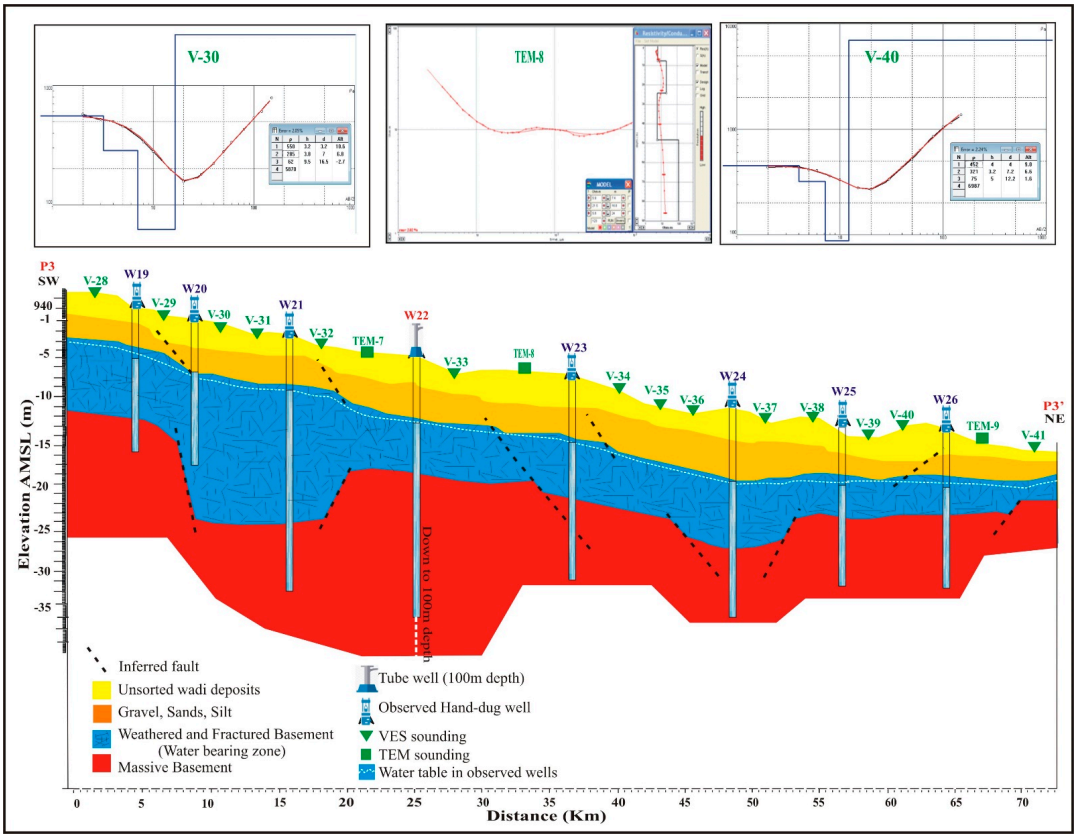

Figure 13. The geoelectric cross-section P3–P3′, with the sounding and the modeled data of VES (V-30, and V-40) and TEM-8.

The interpreted subsurface geoelectrical profiles provide valuable insights into the structural setting, resistivity, thickness, and depths of the aquifer layer. Some specific information that can be obtained from these profiles includes: the presence and distribution of different subsurface materials, such as soil, rock types, and groundwater occurrence; the continuity and discontinuity of stratigraphic units, which may indicate changes in rock types, sedimentary environments, or tectonic activity; the depth and thickness of the aquifer layer, which can inform the feasibility and potential yield of groundwater extraction; and structural features, such as faults, which can affect the distribution and movement of subsurface fluids.

The first geoelectrical cross-section, designated P1–P1′, is located in the upstream area of the wadi channel, which measures approximately 74 km in length (Figure 11). This cross-section includes 12 VESes (V–1 to V–12) and three TDEM soundings (TDEM–1 to TDEM–3). Additionally, there are seven shallow hand-dug wells (W5 to W11) located within this cross-section, ranging in depth from 15 to 16 m. This subsurface profile is characterized by the presence of four distinct geoelectric layers. The top layer is composed of friable soil, made up of unsorted coarse wadi deposits such as sand, silt, and clay, with a resistivity range of 440 to 1020 Ω.m and an average thickness of 1.5 to 4 m. The second layer is made up of gravel and coarse-grained sand, with a resistivity range of 310 to 980 Ω.m and an average thickness of 2.5 to 5 m. The third layer is a water-saturated unit, consisting of gravel, coarse sand, and wadi deposits, as well as the eroded and fractured tops of the basement rocks. It has a resistivity range of 40 to 120 Ω.m and an average thickness of 3 to 7.5 m. The fourth layer extends downward from the aquifer layer to the depth of the soundings and is made up of dry, resistant basement rocks, with a resistivity range of 850 to over 5200 Ω.m.

The second geoelectric profile, P2–P2′, is located in the central part of the Wadi Ranyah mainstream and is characterized by a high slope angle and a total length of 65 Km

(Figure 12). It consists of 15 VESes (V–13 to V–27) and three TDEMs (TEM–4 to TEM–6), as well as one deep tube well (W15) and six shallow hand-dug wells (W12 to W18). The subsurface cross-section of this profile is also made up of four geoelectric layers. The top layer is composed of poorly sorted wadi fills of gravel, sand, and silt, with a resistivity range of 235 to 850 Ω.m and a thickness of 2 to 4 m. The second layer is made up of gravel and coarse sand, with a thickness of 4 to 4.5 m and a resistivity range of 225 to 760 Ω.m. The third layer is characterized by relatively low resistivity values of 65 to 105 Ω.m and is made up of wet, friable, unsorted wadi deposits and the weathered surface of the basement rocks. It has an undulating thickness of 9 to 16 m, particularly beneath the area of the front Wadi Ranyah dam lake and its backside.

It is worth noting that this profile contains the Ranyah Dam in its middle part between V–23 and TEM–6. As a result, the first and second geoelectric layers are very thin, with thicknesses ranging from 0.0 to 0.5 m. The third layer, representing the groundwater saturated zone, is very shallow, with depths ranging from 0.0 to 0.75 m, indicating that the collected surface water in the dam lake has a direct impact on the recharging of the subsurface aquifer layer. The fourth layer is made up of massive basement rocks and is distinguished by high resistivity values ranging from 780 to 4050 Ω.m.

The third geoelectric cross-section, P3–P3′, is located northeast of Ranyah City, on the main channel of Wadi Ranyah near the downstream area and has a total length of approximately 72 km (Figure 13). It consists of 14 VES soundings (V–28 to V–41) and three TEMs (TEM–7 to TEM–9), as well as seven shallow hand-dug wells (W19 to W26) with depths ranging from 15 to 21 m, and one deep tube well (W22) with a depth of 100 m. Similar to the other two subsurface cross-sections along Wadi Ranyah, the first subsurface layer of this cross-section is composed of dry, medium-to-fine gravel, sand, and silt of loose material, with resistivity values ranging from 345 to 985 Ω.m. This layer is thicker towards the downstream area, with a thickness ranging from 3 to 4 m. The second layer is made up of coarse, loose sediments of gravel and sand, with resistivity values ranging from 275 to 740 Ω.m and a thickness of 2.5 to 5 m. The third layer has low resistivity values of 55 to 115 Ω.m and is composed of highly weathered and fractured basement rocks. It has a thickness varying from 8 to 16.5 m. The fourth geoelectric layer is made up of massive, hard basement rocks and has high relative resistivity values varying between 800 to 7850 Ω.m.

4.4. Impact of Structural Elements on the Groundwater Flow and Accumulation

The existence of structural components, such as fractures, faults, and joints, can significantly impact groundwater flow and accumulation in a given region. These characteristics have the potential to produce secondary porosity and high relative permeability, enabling the development of dense, well-connected fracture networks that serve as main pathways for groundwater flow within the subsurface medium. In the case of Wadi Ranyah, surface geology has identified two sets of observed surface-lineament trends, oriented in NW–SE and NE–SW directions, as well as the linear northeast course of the wadi itself (Figure 2). The three constructed geoelectric cross-sections reveal the presence of normal faults dissecting the subsurface strata, particularly within the massive basement rock. Many of these faults are connected to and extend below those visible on the Wadi Ranyah area's surface geological map.

By analyzing the resistivity values, it is possible to detect the downward continuation of faults within the strata. Vertical discontinuities in the resistivity data are frequently used to identify faults, and geoelectric profiles can be used to locate water-bearing zones with low resistivity values. Lateral shifts in resistivity readings may also indicate a boundary contrast between different lithological units, which could be caused by the action of dykes and/or faults in the subsurface. Many of these faults are extensions of surface ones, but some might lie completely underground. These prominent tectonic trends are important in controlling the flow regime of surface-water recharge towards the subsurface strata that make up the shallow groundwater aquifer system. They also control subsurface flow accumulation from upstream to downstream, leading to the formation of isolated,

small, shallow sub-basins along the main channel of Wadi Ranyah that are bounded by major faults.

Profile P1–P1′ provides excellent examples of faulting (Figure 11). Uplifted layers can be seen among VESes 2, 3, 4, 10, and 11, while downward-displaced strata appear among VESes 5, 6, 7, 8, and 9, TDEM–2, VES 11, and TDEM–3. Clearly, these faults interrupt the continuity of the water-bearing zone and serve as groundwater traps at their intersections. Profile P2–P2′ also exhibits significant faulting in the form of a series of parallel step-normal faults that affect the subsurface layers and form a series of small grabens tilting towards the northeast (Figure 12). This feature is clearly visible beneath VESes 22 and 23, TDEM–6, and V–26 and V–27, excluding the region between V–24 and V–25, where the basement rock is uplifted.

In profile P3–P3′, the most prominent feature is the presence of two main basinal reliefs in the central part of the area at V–29, TDEM–7, V–36, and V–38, which provide sufficient thickness for a water-bearing layer (Figure 13). This demonstrates that faults control the flow and storage of groundwater in subsurface medium by acting as barriers.

It is clear that the dense network of surface faults and fractures in the Wadi Ranyah act as conduits for the downward infiltration of surface runoff during rainfall events, resulting in groundwater accumulation in the low-resistivity layer underneath the main channel.

Overall, the three geoelectrical cross-sections along Wadi Ranyah reveal that the wadi is dissected by a series of step-like normal faults that dip towards the downstream area in the northeast. These faults have a significant impact on the groundwater flow regime, as evidenced by the dipping and increasing thickness of the water-bearing zone, which generally trends towards the northeast.

In general, the trend analysis reveals that the primary surface structural trends are in the NW and NE directions, and minor trends in the NS and EW directions were detected from the surface geology map and Landsat data (Figures 2 and 14). The combination of structural patterns on the surface and below may show continuity in the previously mentioned trends within sedimentary strata and basement rocks. Consequently, a connection is formed between the upper Quaternary strata and the lower fractured basement aquifer. This hydraulic connection through the fault lines helps in feeding the aquifer during rainfall events. The NW-trending subsurface fault lines act as barriers for the groundwater flow toward the NE direction. In addition, the northeastward surface runoff is impeded by the surface dams that collect the water in the rainy region in the sub-basin (B) (Figure 4). Therefore, the subsurface fault lines and the surface dams play an essential role in isolating the groundwater bearing layer in the wadi. This is evidenced from the field by the higher differences in groundwater depth along the mainstream of the wadi across the sides of the faults and dykes.

4.5. Hydrogeology and Surface Water

Wadi Ranyah contains a group of hand-dug and tube wells; a total of 26 wells were observed and inventoried along the wadi streams (Figure 1). The primary analysis of these wells water reveals a suitable salinity level ranging from 348 to 785 ppm, and an average discharge rate of 25 to 35 m^3/h. This makes them appropriate according to World Health Organization parameters [90] for meeting domestic needs, such as drinking and irrigation purposes.

The hand-dug wells range in depth from 12 to 30 m, with a width of 5 m and a cement casing with a thickness of 30 cm. The well neck extends 2 m above the ground surface, and the fencing and roof structure is built on top of it. The cement casing extends from 9 to 12 m below the ground, ending at the top of the massive basement rocks, then the borehole continues without casing to the end depth of the well. The two observed tube wells, on the other hand, are 100 m in depth, with a diameter of 12.5 inches and a neck that extends 2 m above the ground surface. The cement casing extends to a depth of 12 m, and screen filters are used to 35 m. The borehole is then sealed with a blank casing and trap to tap the water at the end of the well.

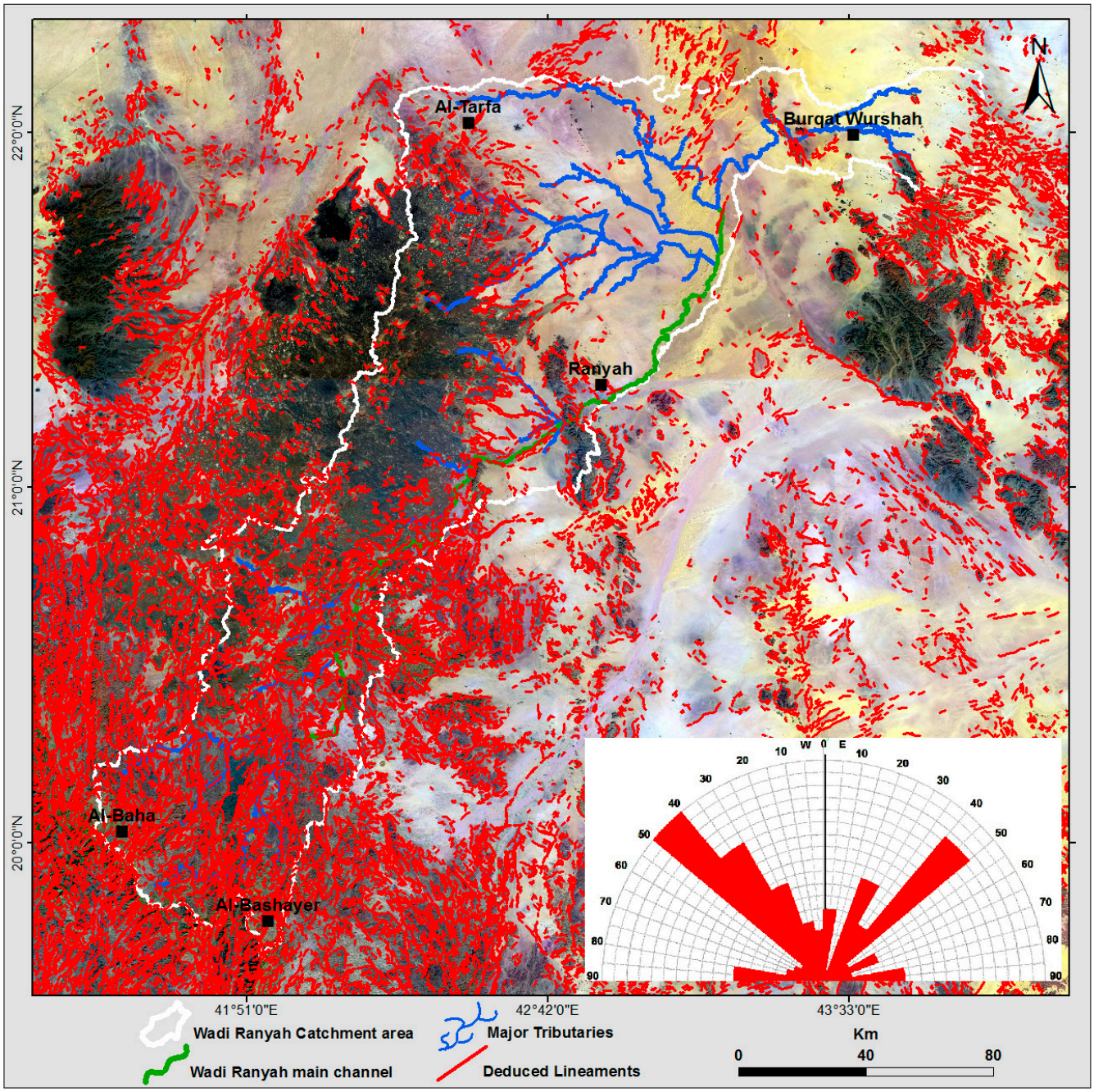

Figure 14. The surface lineaments traced from the Landsat images and its rose diagram for the study region.

The inventoried wells were utilized to assist with the interpretation of resistivity data and reduce uncertainty; some VES and TDEM measurements were taken in the vicinity of 20 existing hand-dug wells and two tube wells. These measurements helped establish correlations and provided additional context for the analysis of the resistivity data.

4.6. Integration of Geophysical Data and Existing Drilled Boreholes

The integration of geophysical data with existing drilled boreholes has been crucial in improving our understanding of the subsurface and revealing the limitations of individual methodologies. In this study, we integrated resistivity data with borehole lithology and hydrogeological information in order to better characterize subsurface hydrogeological features such as bedrock fractures as shown in (Figures 11–13). It is notable that the

subsurface layer thicknesses and water-bearing zones identified through VES and TDEM soundings are in good accordance with the information obtained from the inventoried drilled boreholes along the mainstream of Wadi Ranyah.

4.7. Stream Networks

The slope of Wadi Ranyah's topography is less than 3 percent, where it varies from a higher relief of 1880 m in the upstream region in the southwest to an elevation of around 857 m northeast of Ranyah Village. The stream order of the wadi is seventh (Figure 4). These results were determined using the processed SRTM elevation data with a 30 m spatial resolution (Figure 3). The stream networks discharge a small amount of surface water to the downstream area because of the seven dams that have been constructed to collect surface water in sub-basin (B) close to the upstream area, and the eighth Ranyah dam in the middle part of the wadi (Figures 1 and 4), where precipitation rates are slightly high (Figure 5c). These dams and surface runoff considerably contribute to the replenishment of groundwater, especially near faults in this sub-basin, as shown by the slightly negative GWS values over the southwestern part (Figure 6b). The sub-basin (A) in the downstream region, northeast of Ranyah Village, receives minimal precipitation (Figure 5c). The NS- and NW-trending faults and lineaments produce small, isolated, shallow groundwater reservoirs (Figures 11–13). Consequently, the sub-basin (A) has little groundwater potential in its northeast end segment, compared with the good potentiality of its beginning part near Ranyah Village.

4.8. Comparison with Previous Investigations

GRACE data are currently accessible, with adequate long-term series beginning in 2002, and have been used in many studies. Even though similar studies could be conducted in different places in the southwest of Saudi Arabia, no previous studies have been conducted using our suggested geophysical methods for the Wadi Ranyah region. [37] employed geophysical data to evaluate the regional and local groundwater supplies of Wadi Sar in the Hijaz highlands. They detected a water-bearing layer with low resistivity and variable thickness in the fractured basement rocks of Wadi Sar, and they calculated a general downward trend in groundwater storage variation from April 2002 to July 2017. [91] evaluated the groundwater potential zones in the southwestern part of Makkah city using resistivity, ground-based radar, and topography data. According to their research, groundwater collects in wadis and depressions that are surrounded by faults. [38] used an integrated approach combining geophysical and remote-sensing datasets for a region in southwestern Saudi Arabia, located between longitudes 41.91° and 45.61° and latitudes 17.26° and 19.12°. Their findings indicated that the groundwater shows a depletion trend of -3.4 ± 0.1 mm/yr over the period 2002–2021. The water-bearing unit has a thickness range of 8 to 107 m, and its resistivity is 5.1 to 153 Ω.m. The sedimentary cover and the basement rocks are intersected by three structural trends that run in the NS, NNW, and NNE directions. Other satellite and aerial geophysical field records have been used to investigate crustal characteristics at the continental level [92], Curie point depth and magma chamber's geometry [93], and ground subsidence caused by intense groundwater extraction [94].

5. Conclusions

Due to the low average rainfall rate of 105 mm over the Wadi Ranyah and its occupation by large crystalline basement rocks with thin sedimentary cover, surface-water supplies in the Wadi Ranyah area are generally limited. The region of the wadi shows a decreasing trend in GRACE-derived GWS, estimated at a rate of -3.85 ± 0.15 mm/yr during the study period. Both north–south- and northwest-trending faults extend downward in the underlying fractured and basement rocks, influencing the groundwater flow and occurrences in Wadi Ranyah. The groundwater flowing downstream is impeded by these faults. In addition, the rainfall on the upstream parts is collected by the erected dams, decreasing the downstream surface runoff. Therefore, the surface-water and groundwater resources are

limited. The groundwater seems to occur in fault-controlled zones with substantial recharge in the sub-basin (B) upstream, and with limited recharge at sub-basin (A) downstream. The Wadi Ranyah VESes studies have revealed the existence of four different geoelectrical zones. The unsorted, loose, recently deposited sediments make up the first, more resistant, geoelectrical zone, whereas the second consists of gravel and coarse-grained sands. The third layer is composed of weathered fractured basement rocks as a water-bearing unit, where several northwest–southeast- and north–south-trending faults cut across. Massive basement rocks with higher resistivity values compose the fourth layer. Some fault profiles may have downthrown blocks that operate as traps for groundwater sources. The results of different geophysical datasets are in good agreement for the Wadi Ranyah area.

Author Contributions: Conceptualization, A.M., W.F.G. and A.O.; methodology, A.M., W.F.G. and A.O.; software, A.M., A.O. and W.F.G.; validation, A.M., W.F.G., A.O. and A.A.; formal analysis, A.M., W.F.G., A.O. and A.A.; investigation, A.M. and W.F.G.; resources, A.M., W.F.G. and A.O.; data curation, A.M. and A.O.; writing—original draft preparation, A.M., W.F.G. and A.O.; and writing—review and editing, A.M., W.F.G. and A.O.; visualization, A.M.; supervision, A.M., W.F.G. and A.O.; project administration, A.M.; A.O. and W.F.G.; funding acquisition, A.O. All authors have read and agreed to the published version of the manuscript.

Funding: IFP22UQU4360865DSR245, Deputyship for Research & Innovation, Ministry of Education in Saudi Arabia.

Data Availability Statement: The data is available upon request from the authors.

Acknowledgments: The authors extend their appreciation to the Deputyship for Research & Innovation, Ministry of Education in Saudi Arabia, for funding this research work through the project number: IFP22UQU4360865DSR245.

Conflicts of Interest: The authors declare no conflict of interest.

References

1. Vorosmarty, C.J.; Green, P.; Salisbury, J.; Lammers, R.B. Global Water Resources Vulnerability from Climate Change and Pop-477 ulation Growth. *Science* **2000**, *289*, 284–288. [CrossRef]
2. Immerzeel, W.W.; Beek, L.P.H.v.; Bierkens, M.F.P. Climate change will affect the Asian water towers. *Science* **2010**, *28*, 1382–1385. [CrossRef] [PubMed]
3. Wang, S.; Zhang, M.; Crawford, J.; Hughes, C.E.; Du, M.; Liu, X. The effect of moisture source and synoptic conditions on precipitation isotopes in arid central Asia. *J. Geophys. Res. Atmos.* **2017**, *122*, 2667–2682. [CrossRef]
4. Aljeddani, S.M.A. Forecasting temperature of the Saudi Arabian Province of Makkah using a discrete state–space modeling approach. *J. Umm Al-Qura Univ. Eng. Archit* **2023**. [CrossRef]
5. Rajaee, T.; Ebrahimi, H.; Nourani, V. A review of the artificial intelligence methods in groundwater level modeling. *J. Hydrol.* **2019**, *572*, 336–351. [CrossRef]
6. Wada, Y.; Van Beek, L.P.; Van Kempen, C.M.; Reckman, J.W.; Vasak, S.; Bierkens, M.F. Global depletion of groundwater re-670 sources. *Geophys. Res. Lett.* **2010**, *37*, L20402. [CrossRef]
7. Scanlon, B.R.; Healy, R.W.; Cook, P.G. Choosing appropriate techniques for quantifying groundwater recharge. *Hydrogeol. J.* **2002**, *10*, 18–39. [CrossRef]
8. de Vries, J.J.; Simmers, I. Groundwater recharge: An overview of process and challenges. *Hydrogeol. J.* **2002**, *10*, 5–17. [CrossRef]
9. Milewski, A.; Sultan, M.; Yan, E.; Becker, R.; Abdeldayem, A.; Soliman, F.; Gelil, K.A. A remote sensing solution for estimating runoff and recharge in arid environments. *J. Hydrol.* **2009**, *373*, 1–14. [CrossRef]
10. Wang, J.; Song, C.; Reager, J.T.; Yao, F.; Famiglietti, J.S.; Sheng, Y.; MacDonald, G.M.; Brun, F.; Schmied, H.M.; Marston, R.A.; et al. Recent global decline in endorheic basin water storages. *Nat. Geosci.* **2018**, *11*, 926–932. [CrossRef]
11. Mohamed, A.; Ahmed, E.; Alshehri, F.; Abdelrady, A. The groundwater flow behavior and the recharge in the Nubian Sandstone Aquifer System during the wet and arid periods. *Sustainability* **2022**, *14*, 6823. [CrossRef]
12. Mohamed, A.; Asmoay, A.; Alshehri, F.; Abdelrady, A.; Othman, A. Hydro-geochemical applications and multivariate analysis to assess the water–rock interaction in arid environments. *Appl. Sci.* **2022**, *12*, 6340. [CrossRef]
13. Mohamed, A.; Sultan, M.; Ahmed, M.; Yan, E.; Ahmed, E. Aquifer recharge, depletion, and connectivity: Inferences from GRACE, land surface models, and geochemical and geophysical data. *Bull. Geol. Soc. Am.* **2017**, *129*, 534–546. [CrossRef]
14. Mohanty, S.; Jha, M.K.; Kumar, A.; Sudheer, K. Artificial neural network modeling for groundwater level forecasting in a river 678 island of eastern India. *Water Resour. Manag.* **2010**, *24*, 1845–1865. [CrossRef]

15. Wagena, M.B.; Goering, D.; Collick, A.S.; Bock, E.; Fuka, D.R.; Buda, A.; Easton, Z.M. Comparison of short-term streamflow 680 forecasting using stochastic time series, neural networks, process-based, and Bayesian models. *Environ. Model. Softw.* **2020**, *126*, 104669. [CrossRef]
16. Su, T.; Miao, C.; Duan, Q.; Gou, J.; Guo, X.; Zhao, X. Hydrological response to climate change and human activities in the Three-River Source Region. *Hydrol. Earth Syst. Sci. Discuss.* 2022; in review. [CrossRef]
17. Oberndorfer, H.; Miiller, J.; Rummel, R.; Sneeuw, N. A simulation tool for the new gravity field satellite missions. *Adv. Space Res.* **2002**, *30*, 227–232. [CrossRef]
18. Swenson, S.; Wahr, J. Methods for inferring regional surface-mass anomalies from Gravity Recovery and Climate Experiment 494 (GRACE) measurements of time-variable gravity. *J. Geophys. Res.* **2002**, *107*, 2193. [CrossRef]
19. Chao, B.F.; Liau, J.R. Gravity Changes Due to Large Earthquakes Detected in GRACE Satellite Data via Empirical Orthogonal 496 Function Analysis. *J. Geophys. Res. Solid Earth* **2019**, *124*, 3024–3035. [CrossRef]
20. Tang, L.; Li, J.; Chen, J.; Wang, S.-Y.; Wang, R.; Hu, X. Seismic Impact of Large Earthquakes on Estimating Global Mean Ocean 500 Mass Change from GRACE. *Remote Sens.* **2020**, *12*, 935. [CrossRef]
21. Velicogna, I.; Wahr, J. Measurements of Time Variable Gravity Show Mass Loss in Antarctica. *Science* **2006**, *311*, 1754–1756. [CrossRef]
22. Luthcke, S.B.; Zwally, H.J.; Abdalati, W.; Rowlands, D.D.; Ray, R.D.; Nerem, R.S.; Lemoine, F.G.; McCarthy, J.J.; Chinn, D.S. Recent Greenland ice mass loss by drainage system from satellite gravity observations. *Science* **2006**, *314*, 1286–1289. [CrossRef] [PubMed]
23. Mohamed, A.; Sultan, M.; Yan, E.; Ahmed, E.; Sturchio, N.C. Towards a Better Understanding of the Hydrologic Setting of the Nubian Sandstone Aquifer System: Inferences from Groundwater Flow Models, CL-36 Ages, and GRACE Data. 2015. AGU Fall Meeting Abstracts, San Francisco. Available online: https://www.researchgate.net/publication/289538910_Towards_a_better_understanding_of_the_hydrologic_setting_of_the_Nubian_Sandstone_Aquifer_System_Inferences_from_groundwater_flow_models_Cl-36_ages_and_GRACE_data (accessed on 16 March 2023).
24. Fallatah, O.A.; Ahmed, M.; Save, H.; Akanda, A.S. Quantifying Temporal Variations in Water Resources of a Vulnerable Middle Eastern Transboundary Aquifer System. *Hydrol. Process* **2017**, *31*, 4081–4091. [CrossRef]
25. Fallatah, O.A.; Ahmed, M.; Cardace, D.; Boving, T.; Akanda, A.S. Assessment of Modern Recharge to Arid Region Aquifers Using an Integrated Geophysical, Geochemical, and Remote Sensing Approach. *J. Hydrol.* **2019**, *569*, 600–611. [CrossRef]
26. Mohamed, A. Gravity based estimates of modern recharge of the Sudanese area. *J. Afr. Earth Sci.* **2020**, *163*, 103740. [CrossRef]
27. Mohamed, A. Gravity applications to groundwater storage variations of the Nile Delta Aquifer. *J. Appl. Geophys.* **2020**, *182*, 104177. [CrossRef]
28. Mohamed, A.; Ragaa Eldeen, E.; Abdelmalik, K. Gravity based assessment of spatio-temporal mass variations of the groundwater resources in the Eastern Desert, Egypt. *Arab. J. Geosci.* **2021**, *14*, 500. [CrossRef]
29. Mohamed, A.; Gonçalvès, J. Hydro-geophysical monitoring of the North Western Sahara Aquifer System's groundwater resources using gravity data. *J. Afr. Earth Sci.* **2021**, *178*, 104188. [CrossRef]
30. Alshehri, F.; Mohamed, A. Analysis of Groundwater Storage Fluctuations Using GRACE and Remote Sensing Data in Wadi As-Sirhan, Northern Saudi Arabia. *Water* **2023**, *15*, 282. [CrossRef]
31. Mohamed, A. Hydro-geophysical study of the groundwater storage variations over the Libyan area and its connection to the Dakhla basin in Egypt. *J. Afr. Earth Sci.* **2019**, *157*, 103508. [CrossRef]
32. Mohamed, A. Gravity applications in estimating the mass variations in the Middle East: A case study from Iran. *Arab. J. Geosci.* **2020**, *13*, 364. [CrossRef]
33. Othman, A.; Abdelrady, A.; Mohamed, A. Monitoring Mass Variations in Iraq Using Time-Variable Gravity Data. *Remote Sens.* **2022**, *14*, 3346. [CrossRef]
34. Mohamed, A.; Abdelrahman, K.; Abdelrady, A. Application of Time-Variable Gravity to Groundwater Storage Fluctuations in Saudi Arabia. *Front. Earth Sci.* **2022**, *10*, 873352. [CrossRef]
35. Mohamed, A.; Faye, C.; Othman, A.; Abdelrady, A. Hydro-geophysical Evaluation of the Regional Variability of Senegal's Terrestrial Water Storage Using Time-Variable Gravity Data. *Remote Sens.* **2022**, *14*, 4059. [CrossRef]
36. Mohamed, A.; Abdelrady, A.; Alarifi, S.S.; Othman, A. Geophysical and Remote Sensing Assessment of Chad's Groundwater Resources. *Remote Sens.* **2023**, *15*, 560. [CrossRef]
37. Taha, A.I.; Al Deep, M.; Mohamed, A. Investigation of groundwater occurrence using gravity and electrical resistivity methods: A case study from Wadi Sar, Hijaz Mountains, Saudi Arabia. *Arab. J. Geosci.* **2021**, *14*, 334. [CrossRef]
38. Mohamed, A.; Al Deep, M.; Othman, A.; Taha, A.L.; Alshehri, F.; Abdelrady, A. Integrated Geophysical Assessment of groundwater potential in southwestern Saudi Arabia. *Front. Earth Sci.* **2022**, *10*, 937402. [CrossRef]
39. Wang, Z.; Zhang, B.; Jiang, W.; Che, G. Ocean Mass Variations in the South China Sea Inferred from Satellite Altimetry, GRACE, Oceanographic and Meteorological Data. *Geomat. Inf. Sci. Wuhan Univ.* **2018**, *508*, 571–578, (In Chinese Abstract).
40. Royston, S.; Dutt Vishwakarma, B.; Westaway, R.; Rougier, J.; Sha, Z.; Bamber, J. Can We Resolve the Basin-Scale Sea Level 512 Trend Budget from GRACE Ocean Mass? *J. Geophys. Res. Ocean.* **2020**, *125*, e2019JC015535. [CrossRef]
41. Rodell, M.; Famiglietti, J.S.; Wiese, D.N.; Reager, J.T.; Beaudoing, H.K.; Landerer, F.W.; Lo, M.H. Emerging trends in global freshwater availability. *Nature* **2018**, *557*, 651–659. [CrossRef]
42. Amery, H.A.; Wolf, A.T. *Water in the Middle East: A Geography of Peace*; University of Texas Press: Austin, TX, USA, 2000.

43. Wolf, A.T.; Newton, J.T. Case Study Transboundary Dispute Resolution: The Tigris-Euphrates Basin. Oregon State University, Transboundary Freshwater Dispute Database (TFDD). 2007. Available online: http://www.transboundarywaters.orst.edu/ (accessed on 7 December 2022).
44. Wolf, A. Conflict and cooperation along international waterways. *Water Policy* **1998**, *1*, 251–265. [CrossRef]
45. Al-Ibrahim, A.A. Excessive use of groundwater resources in Saudi Arabia: Impacts and policy options. *AMBIO* **1992**, *20*, 34–37.
46. FAO. Saudi Arabia. Irrigation in the Middle East regions in figures. Aquastat Survey, 2008. In *FAO Land and Water Division Report 34*; Freken, K., Ed.; FAO: Rome, Italy, 2009; pp. 325–337.
47. Hassan, R.A.; Almatani, T.U. Assessment of radon levels in groundwater in the city of Makkah, KSA. *J. Umm Al-Qura Univ. Appl. Sci.* **2022**, *8*, 2–7. [CrossRef]
48. Ouda, O.K.M. Water demand versus supply in Saudi Arabia: Current and future challenges. *Int. J. Water Resour. Dev.* **2014**, *30*, 335–344. [CrossRef]
49. General Authority of Statistics, Sustainable Development Goals in the Kingdom of Saudi Arabia. Report; 2019. Available online: https://www.stats.gov.sa/ (accessed on 7 December 2022).
50. Water Challenges in KSA. Fanack Water. 20 June 2021. Available online: water.fanack.com/saudi-arabia/water-challenges-in-ksa (accessed on 7 December 2022).
51. Dahlin, T.; Bjelm, L.; Svensson, C. Use of Electrical Imaging in Site Investigations for a Railway Tunnel through the Hallandsås Horst, Sweden. *Q. J. Eng. Geol. Hydrogeol.* **1999**, *32*, 163–172. [CrossRef]
52. Muchingami, I.; Hlatywayo, D.J.; Nel, J.M.; Chuma, C. Electrical resistivity survey for groundwater investigations and shallow subsurface evaluation of the basaltic-greenstone formation of the urban Bulawayo aquifer. *Phys. Chem. Earth* **2012**, *50–52*, 44–51. [CrossRef]
53. Reynolds, J.M. *An Introduction to Applied and Environmental Geophysics*; John Wiley and Sons Ltd.: Chichester, UK, 1997; 796p.
54. Choudhury, K.; Saha, D.K.; Chakraborty, P. Geophysical Study for Saline Water Intrusion in a Coastal Alluvial Terrain. *J. Appl. Geophys.* **2001**, *46*, 189–200. [CrossRef]
55. Frohlich, R.K.; Kelly, W.E. Estimates of Specific Yield with the Geoelectric Resistivity Method in Glacial Aquifers. *J. Hydrol.* **1988**, *97*, 33–44. [CrossRef]
56. Troisi, S.; Fallico, C.; Straface, S.; Migliari, E. Application of Kriging with External Drift to Estimate Hydraulic Conductivity from Electrical-Resistivity Data in Unconsolidated Deposits Near Montalto Uffugo, Italy. *Hydrogeol. J.* **2000**, *8*, 356–367. [CrossRef]
57. Kessels, W.; Flentge, I.; Kolditz, H. Dc Geoelectric Sounding to Determine Water Content in the Salt Mine Asse (FRG). *Geophys. Prospect.* **1985**, *33*, 446–456. [CrossRef]
58. Raju, N.; Reddy, T. Fracture pattern and electrical resistivity studies for groundwater exploration. *Environ. Geol.* **1998**, *34*, 175–182. [CrossRef]
59. Chandra, S.; Nagaiah, E.; Reddy, D.V.; Rao, V.A.; Ahmed, S. Exploring Deep Potential Aquifer in Water Scarce Crystalline Rocks. *J. Earth Syst. Sci.* **2012**, *121*, 1455–1468. [CrossRef]
60. ALDeep, M.; Araffa, S.A.S.; Mansour, S.A.; Taha, A.I.; Mohamed, A.; Othman, A. Geophysics and remote sensing applications for groundwater exploration in fractured basement: A case study from Abha area, Saudi Arabia. *J. Afr. Earth Sci.* **2021**, *184*, 104368. [CrossRef]
61. Karlik, G.; Kaya, M.A. Investigation of Groundwater Contamination Using Electric and Electromagnetic Methods at an Open Waste Disposal Site: A Case Study from Isparta, Turkey. *Environ. Geol.* **2001**, *40*, 725–731. [CrossRef]
62. Ebong, E.D.; Akpan, A.E.; Onwuegbuche, A.A. Estimation of Geohydraulic Parameters from Fractured Shales and Sandstone Aquifers of Abi (Nigeria) Using Electrical Resistivity and Hydrogeologic Measurements. *J. Afr. Earth Sci.* **2014**, *96*, 99–109. [CrossRef]
63. Christiansen, A.V.; Auken, E.; Sorensen, K. The Transient Electromagnetic Method. In *Groundwater Geophysics—A Tool for Hydrogeology*; Kirsch, R., Ed.; GSW Ltd.: Aarhus, Denmark, 2006; pp. 179–225. [CrossRef]
64. Brown, G.F.; Jackson, R.O. Geologic Map of the Asir Quadrangle, Kingdom of Saudi Arabia. In U.S. Geological Survey Miscellaneous Geologic Investigations Map I-217A: Scale: 1:500,000; 1979. USGS Publications Warehouse. Available online: http://pubs.er.usgs.gov/publication/i217A (accessed on 7 December 2022).
65. Gao, F.; Wang, H.; Liu, C. Long-term assessment of groundwater resources carrying capacity using GRACE data and Budyko 760 model. *J. Hydrol.* **2020**, *58*, 125042. [CrossRef]
66. Save, H.; Bettadpur, S.; Tapley, B.D. High-resolution CSR GRACERL05 Mascons. *J. Geophys. Res. Solid Earth* **2016**, *121*, 7547–7569. [CrossRef]
67. Save, H. CSR GRACE and GRACE-FO RL06 Mascon Solutions v02. *Mascon Solut.* **2020**, *12*, 24. [CrossRef]
68. Watkins, M.M.; Wiese, D.N.; Yuan, D.-N.; Boening, C.; Landerer, F.W. Improved methods for observing Earth's time variable mass distribution with GRACE using spherical cap mascons. *J. Geophys. Res. Solid Earth* **2015**, *120*, 2648–2671. [CrossRef]
69. Wiese, D.N.; Landerer, F.W.; Watkins, M.M. Quantifying and reducing leakage errors in the JPL RL05M GRACE mascon solution. *Water Resour. Res.* **2016**, *52*, 7490–7502. [CrossRef]
70. Landerer, F.W.; Flechtner, F.M.; Save, H.; Webb, F.H.; Bandikova, T.; Bertiger, W.I.; Bettadpur, S.V.; Byun, S.H.; Dahle, C.; Dobslaw, H.; et al. Extending the Global Mass Change Data Record: GRACE Follow-On Instrument and Science Data Performance. *Geophys. Res. Lett.* **2020**, *47*, e2020GL088306. [CrossRef]

71. Luthcke, S.B.; Sabaka, T.J.; Loomis, B.D.; Arendt, A.A.; McCarthy, J.J.; Camp, J. Antarctica, Greenland, and Gulf of Alaska land-ice evolution from an iterated GRACE global mascon solution. *J. Glaciol.* **2013**, *59*, 216. [CrossRef]
72. Ahmed, M.; Abdelmohsen, K. Quantifying modern recharge and depletion rates of the Nubian aquifer in Egypt. *Surv. Geophys.* **2018**, *39*, 729–751. [CrossRef]
73. Shamsudduha, M.; Taylor, R.G.; Longuevergne, L. Monitoring groundwater storage changes in the highly seasonal humid tropics: Validation of GRACE measurements in the Bengal Basin. *Water Resour. Res.* **2012**, *48*, W02508. [CrossRef]
74. Rodell, M.; Houser, P.R.; Jambor, U.; Gottschalck, J.; Mitchell, K.; Meng, C.-J.; Arsenault, K.; Cosgrove, B.; Radakovich, J.; Bosilovich, M.; et al. The Global Land Data Assimilation System. *Bull. Am. Meteorol. Soc.* **2004**, *85*, 381–394. [CrossRef]
75. Akingboye, A.S.; Bery, A.A.; Kayode, J.S.; Asulewon, A.M.; Bello, R.; Agbasi, O.E. Near-Surface Crustal Architecture and Geohydrodynamics of the Crystalline Basement Terrain of Araromi, Akungba-Akoko, SW Nigeria, Derived from Multi-Geophysical Methods. *Nat. Resour. Res.* **2022**, *31*, 215–236. [CrossRef]
76. McLachlan, P.; Blanchy, G.; Chambers, J.; Sorensen, J.; Uhlemann, S.; Wilkinson, P.; Binley, A. The application of electromagnetic induction methods to reveal the hydrogeological structure of a riparian wetland. *Water Resour. Res.* **2021**, *57*, e2020WR029221. [CrossRef]
77. Ren, Z.; Kalscheuer, T. Uncertainty and Resolution Analysis of 2D and 3D Inversion Models Computed from Geophysical Electromagnetic Data. *Surv. Geophys.* **2020**, *41*, 47–112. [CrossRef]
78. Constable, S.C.; Parker, R.L.; Constable, C.G. Occam's inversion: A practical algorithm for generating smooth models from electromagnetic sounding data. *Geophysics* **1987**, *52*, 289–300. [CrossRef]
79. Bobachev, A.A. IPI2WIN Program 2005, Version 3.1 2: 17. 10. 08 (1990–2008) Copyright al 1990; Programs set for VEs data interofretion. Dep. Geophysics, Geological Fac. Moseeow State VnV. Fussow, 119899. Available online: https://ijiset.com/vol2/v2s12/IJISET_V2_I12_59.pdf (accessed on 7 December 2022).
80. TEM-Researcher Software, Version 7; Applied Electromagnetic Research (AEMR); The Netherlands, 2007. p. 49. Available online: https://scirp.org/reference/referencespapers.aspx?referenceid=1404300 (accessed on 7 December 2022).
81. USGS. The United States Geological Survey, Earth Resources Observation and Science Data Centre (EROS). 2022. Available online: http://eros.usgs.gov (accessed on 7 December 2022).
82. SRTM. National Aeronautics and Space Administration (NASA) Topography, Shuttle Radar Topography Mission. USA; 2013. Available online: https://www.usgs.gov/centers/eros/science/usgs-eros-archive-digital-elevation-shuttle-radar-topography-mission-srtm-1 (accessed on 7 December 2022).
83. Jamal, S.; Ali, A. A comparative study of automatic drainage network extraction using ASTER GDEM, SRTM DEM and Cartosat-1 DEM in parts of Kosi basin, Bihar, India. *J. Umm Al-Qura Univ. Eng. Archit.* **2023**. [CrossRef]
84. Anwar, A.; Shawki, N.; Abdoh, G. Landsat ETM-7 for LineamentMappingUsing Automatic Extraction Technique in the SWPart of Taiz Area, Yemen. *Glob. J. Hum. Soc. Sci. Geogr. Geo-Sci. Environ. Disaster Manag.* **2013**, *13*, 35.
85. *Geomatica PCI*; PCI Geomatics Enterprises, Inc.: Markham, ON, Canada, 2018; p. 6H3.
86. ESRI. *ArcGIS 10.5 Desktop*; Environmental System Research Institute, Inc.: Redlands, CA, USA, 2017.
87. Rodell, M.; Chen, J.; Kato, H.; Famiglietti, J.S.; Nigro, J.; Wilson, C.R. Estimating groundwater storage changes in the Mississippi River basin (USA) using GRACE. *Hydrogeol. J.* **2009**, *15*, 159–166. [CrossRef]
88. Gonçalvès, J.; Petersen, J.; Deschamps, P.; Hamelin, B.; Baba-Sy, O. Quantifying the modern recharge of the "fossil" Sahara aquifers. *Geophys. Res. Lett.* **2013**, *40*, 2673–2678. [CrossRef]
89. Bhanja, S.N.; Mukherjee, A.; Rodell, M. Groundwater storage variations in India. In *Groundwater of South Asia*; Mukherjee, A., Ed.; Springer: Singapore, 2018; pp. 49–59.
90. World Health Organization (WHO). Guidelines for Drinking-Water Quality: Fourth Edition Incorporating the First and Second Addenda. 2022. Available online: https://www.who.int/publications/i/item/9789240045064 (accessed on 3 February 2023).
91. Morsy, E.A.; Othman, A. Delineation of Shallow Groundwater Potential Zones Using Integrated Hydrogeophysical and Topographic Analyses, Western Saudi Arabia. *J. King Saud Univ. Sci.* **2021**, *33*, 101559. [CrossRef]
92. Mohamed, A.; Al Deep, M. Depth to the Bottom of the Magnetic Layer, Crustal Thickness, and Heat Flow in Africa: Inferences from Gravity and Magnetic Data. *J. Afr. Earth Sci.* **2021**, *179*, 104204. [CrossRef]
93. Mohamed, A.; Al Deep, M.; Abdelrahman, K.; Abdelrady, A. Geometry of the magma chamber and curie point depth beneath Hawaii Island: Inferences from magnetic and gravity data. *Front. Earth Sci.* **2022**, *10*, 847984. [CrossRef]
94. Othman, A. Measuring and Monitoring Land Subsidence and Earth Fissures in Al-Qassim Region, Saudi Arabia: Inferences from InSAR. In *Advances in Remote Sensing and Geo Informatics Applications, Proceedings of the Conference of the Arabian Journal of Geosciences, CAJG 2018, Hammamet, Tunisia, 12–15 November 2018*; El-Askary, H., Lee, S., Heggy, E., Pradhan, B., Eds.; Advances in Science, Technology & Innovation (IEREK Interdisciplinary Series for Sustainable Development); Springer: Cham, Switzerland, 2019.